

A Numerical Study of the Cosmic Microwave Background

AST5220 - Cosmology II

Candidate 15011

Institute of Theoretical Astrophysics (ITA), University of Oslo

March 25, 2025

ABSTRACT

Context. CONTEXT

Aims. AIMS

Methods. METHODS

Results. RESULTS

Conclusions. CONCLUSIONS

Key words. cosmic background radiation - large-scale structure of Universe

1. Introduction

TODO: proper intro when finished

In this work, I extensively reference the 2018 Planck results (see [Planck Collaboration et al. 2020](#)), which serve as the fiducial cosmology. The theoretical framework for this study, including derivations and discussions, is based on material from the AST5220 - Cosmology II course taught by Hans A. Winther at the University of Oslo (see [Winther et al. Accessed: February 2025](#)). All computational codes used in this work are available on my [GitHub repository](#), with major components based on templates developed by Winther.

2. Milestone I: Background Cosmology

The evolution of the universe is governed by the interplay between different energy components, including radiation, matter, and dark energy. Understanding how these components influence the expansion history is essential for predicting the large-scale structure of the Universe and the Cosmic Microwave Background (CMB) fluctuations. This milestone focuses on modeling the background evolution of the Universe using the Friedmann equations, which describe how the Hubble parameter H , and thus time and distance measures, evolve with redshift.

I implement a numerical framework that takes in cosmological parameters and computes such key background quantities, and use this to fit to measurements of supernova luminosity distances. By completing this milestone, I aim to establish a robust computational framework that serves as a foundation for later stages of the project, where I analyze perturbations and extract information about CMB anisotropies to obtain constraints on cosmological parameters. TODO: maybe change

2.1. Theoretical framework

2.1.1. Evolution of the Universe and the Hubble parameter

The expansion of the Universe is governed by General Relativity, with the large-scale dynamics described by the Friedmann-Lemaître-Robertson-Walker (FLRW) metric. Assuming a homo-

geneous and isotropic universe, the metric is given by

$$ds^2 = -c^2 dt^2 + a^2(t) \left[\frac{dr^2}{1 - kr^2} + r^2 d\theta^2 + r^2 \sin^2 \theta d\phi^2 \right], \quad (2.1)$$

where $a(t) = 1/(1+z)$ is the dimensionless scale factor, with z being the cosmological redshift. The constant k determines the curvature of the Universe ($k = 0$ for a flat universe, $k > 0$ for a closed universe, and $k < 0$ for an open universe).

The evolution of $a(t)$ is governed by the Friedmann equation, which is derived from Einstein's field equations:

$$H^2 = \frac{8\pi G}{3} \sum_i \rho_i - \frac{kc^2}{a^2} \simeq \frac{8\pi G}{3} \sum_i \rho_i, \quad (2.2)$$

Here, $H = \dot{a}/a$ is the Hubble parameter, and ρ_i denotes the total energy density of some component (photons, baryons, etc.). In the second equality I have used that we can treat the curvature as its own component that is included in the sum, with energy density

$$\rho_k = -\frac{3}{8\pi G} \frac{kc^2}{a^2}. \quad (2.3)$$

It is essential to know not only how the curvature “energy density” scales with a , but the other components as well. To understand this, we start with the continuity equation for a perfect fluid, which is a very accurate description of the energy density components in the Universe on the largest scales, applied to a homogeneous and isotropic universe:

$$\frac{d\rho_i}{dt} + 3H(\rho_i + p_i) = \frac{d\rho_i}{dt} + \frac{3}{a} \frac{da}{dt} \rho_i (1 + w_i) = 0. \quad (2.4)$$

Here, p_i is the pressure of the fluid, and $w_i = p_i/\rho_i$ is the equation of state parameter, which is constant for the fluids considered in conventional cosmology. This differential equation is easily solved by separating variables and integrating, which gives us:

$$\rho_i(a) = \rho_{i0} a^{-3(1+w_i)}, \quad (2.5)$$

where ρ_{i0} is the present-day density.

On large scales, non-relativistic matter can essentially be treated as pressureless, hence $w_m = w_b = w_{\text{CDM}} = 0$ and thus

$\rho_m \propto a^{-3}$. This corresponds to the dilution of a density field in an expanding volume. Furthermore, neutrinos are so light that they can still be treated as relativistic (radiation), and we therefore have $w_r = w_\gamma = w_\nu = 1/3$, which implies $\rho_r \propto a^{-4}$. Radiation is also diluted as the Universe expands, and the extra factor of a^{-1} comes from redshifting of relativistic particles in an expanding universe. From eq. (2.3) we indeed see that we can treat curvature as a perfect fluid with equation of state $w_k = -1/3$, while dark energy, represented by the cosmological constant Λ , remains constant in time, hence $w_\Lambda = -1$.

A much more convenient way of writing the Friedmann equation can be derived by defining the critical density, which is the density required for a flat universe ($k = 0$):

$$\rho_c = \frac{3H^2}{8\pi G}. \quad (2.6)$$

We may then define the dimensionless density parameters, which describe how much of the total energy density each component i contributes:

$$\Omega_i = \frac{\rho_i}{\rho_c}. \quad (2.7)$$

Substituting this into the Friedmann equation gives us then

$$H^2 = \frac{8\pi G}{3} \sum_i \Omega_i \rho_c = H^2 \sum_i \Omega_i, \quad (2.8)$$

which shows us explicitly that the density parameters always must sum up to unity. We would like to rewrite this in terms of quantities that we can actually measure today, such as the present day density parameters Ω_{i0} . In that case, H^2 becomes H_0^2 on the right-hand side of eq. (2.8). Furthermore, since we know how the density components scale with a , we may write

$$H^2 = H_0^2 \sum_i \Omega_{i0} a^{-3(1+w_i)}. \quad (2.9)$$

The equivalency of this expression with eq. (2.8) tells us that

$$\Omega_i(a) = \frac{\Omega_{i0} a^{-3(1+w_i)}}{H^2(a)/H_0^2}, \quad (2.10)$$

Additionally, taking the square root on both sides of eq. (2.9) and writing out the terms explicitly, we have

$$H = H_0 \sqrt{(\Omega_{b0} + \Omega_{\text{CDM}0})a^{-3} + (\Omega_{\gamma0} + \Omega_{\nu0})a^{-4} + \Omega_{k0}a^{-2} + \Omega_{\Lambda0}}. \quad (2.11)$$

When fitting to measurements of supernova luminosity distances, I attempt to constrain all but the photon and neutrino density parameters. This is because we know these are given by

$$\Omega_{\gamma0} = g \frac{\pi^2 (k_B T_{\text{CMB}0})^4}{30 \hbar^3 c^5} \frac{8\pi G}{3H_0^2}, \quad (2.12)$$

$$\Omega_{\nu0} = \frac{7}{8} N_{\text{eff}} \left(\frac{4}{11} \right)^{1/3} \Omega_{\gamma0}. \quad (2.13)$$

where $g = g_\gamma = g_\nu = 2$, since photons and neutrinos both have 2 internal polarization states. We see that the only free parameters that appear in these expressions are $T_{\text{CMB}0}$, the present day value of the CMB temperature, and N_{eff} , the effective number of relativistic degrees of freedom, both of which are determined to high precision already.

When integrating from the very early universe, using the scale factor a as the time parameter becomes numerically challenging, as it rapidly decreases to vanishingly small values. To address this, I therefore adopt the logarithmic time coordinate

$$x = \log a, \quad (2.14)$$

instead, which implies that $x = 0$ today and $x = -\infty$ at the Big Bang. Expressed in terms of $\Omega_{m0} = \Omega_{b0} + \Omega_{\text{CDM}0}$ and $\Omega_{r0} = \Omega_{\gamma0} + \Omega_{\nu0}$, we can equivalently write the Hubble parameter as

$$H = H_0 \sqrt{\Omega_{m0} e^{-3x} + \Omega_{r0} e^{-4x} + \Omega_{k0} e^{-2x} + \Omega_{\Lambda0}}. \quad (2.15)$$

A commonly used rescaled version of the Hubble parameter is the conformal Hubble parameter:

$$\mathcal{H} = aH = H_0 \sqrt{\Omega_{m0} e^{-x} + \Omega_{r0} e^{-2x} + \Omega_{k0} + \Omega_{\Lambda0} e^{2x}}. \quad (2.16)$$

This naturally appears when rewriting cosmological equations in terms of the conformal time η , which I present below. I focus more on this version of the Hubble parameter, partly because its first and second derivatives with respect to x prove themselves useful verifying the validity of approximations I make later on. After some tedious calculation, we find that these are

$$\begin{aligned} \frac{d\mathcal{H}}{dx} &= \frac{H_0}{2} \frac{-\Omega_{m0} e^{-x} - 2\Omega_{r0} e^{-2x} + 2\Omega_{\Lambda0} e^{2x}}{\sqrt{\Omega_{m0} e^{-x} + \Omega_{r0} e^{-2x} + \Omega_{k0} + \Omega_{\Lambda0} e^{2x}}}, \\ &= -\frac{H_0^2}{2\mathcal{H}} (\Omega_{m0} e^{-x} + 2\Omega_{r0} e^{-2x} - 2\Omega_{\Lambda0} e^{2x}), \\ \frac{d^2\mathcal{H}}{dx^2} &= \frac{H_0}{2} \left(\frac{\Omega_{m0} e^{-x} + 4\Omega_{r0} e^{-2x} + 4\Omega_{\Lambda0} e^{2x}}{\sqrt{\Omega_{m0} e^{-x} + \Omega_{r0} e^{-2x} + \Omega_{k0} + \Omega_{\Lambda0} e^{2x}}} \right. \\ &\quad \left. - \frac{1}{2} \frac{(\Omega_{m0} e^{-x} + 2\Omega_{r0} e^{-2x} - 2\Omega_{\Lambda0} e^{2x})^2}{(\Omega_{m0} e^{-x} + \Omega_{r0} e^{-2x} + \Omega_{k0} + \Omega_{\Lambda0} e^{2x})^{3/2}} \right), \\ &= \frac{H_0^2}{\mathcal{H}} \left[\frac{1}{2} \Omega_{m0} e^{-x} + 2\Omega_{r0} e^{-2x} + 2\Omega_{\Lambda0} e^{2x} - \frac{1}{H_0^2} \left(\frac{d\mathcal{H}}{dx} \right)^2 \right]. \end{aligned} \quad (2.17)$$

maybe move to appendix

2.1.2. Conformal time and distance measures

The cosmic time t is related to our time variable x through

$$\frac{dt}{dx} = \frac{dt}{da} \frac{da}{dx} = \frac{a}{\dot{a}} = \frac{1}{H}, \quad (2.19)$$

hence, to compute the cosmic time t given our time coordinate x , we simply integrate this to get

$$t(x) = \int_{-\infty}^x \frac{dx'}{H(x')}. \quad (2.20)$$

Evaluating this at $x = 0$ (today), we obtain the age of the Universe.

While it is interesting to solve our system of equations for t , it is more useful to introduce the conformal time η . This is defined as

$$d\eta = \frac{cdt}{a} \Leftrightarrow \frac{d\eta}{dx} = \frac{c}{\mathcal{H}}, \quad (2.21)$$

and thus has units of length. The equation on the right can easily be numerically integrated to obtain $\eta(x)$, which describes how far

light has traveled since the Big Bang. It is therefore also called the particle horizon, and is a crucial concept in cosmology, as it determines the causal structure of the Universe.

A closely related quantity is the so-called comoving distance a photon has travelled since emission, defined as

$$\chi = \eta_0 - \eta, \quad (2.22)$$

where η_0 is the conformal time today. This is fundamental in defining distance measures in cosmology. We know that photons travel along null geodesics $ds^2 = 0$, and from the conformal time and the FLRW line element we see that this implies that the coordinate distance r satisfies

$$cdt = \frac{adr}{\sqrt{1 - kr^2}}, \quad (2.23)$$

for a radially traveling photon ($d\theta = d\phi = 0$). Changing the time coordinate to conformal time, we rewrite this as

$$d\eta = \frac{dr}{\sqrt{1 - kr^2}}, \quad (2.24)$$

and integrating from emission at time η to today, we get precisely the comoving distance:

$$\int_{\eta}^{\eta_0} d\eta' \equiv \chi = \int_0^r \frac{dr'}{\sqrt{1 - kr'^2}}. \quad (2.25)$$

Solving this integral for different values of the curvature constant k , we obtain

$$r = \chi \begin{cases} \frac{\sin(\sqrt{|\Omega_{k0}|}H_0\chi/c)}{(\sqrt{|\Omega_{k0}|}H_0\chi/c)}, & \Omega_{k0} < 0 \quad (\text{Closed}), \\ 1, & \Omega_{k0} = 0 \quad (\text{Flat}), \\ \frac{\sinh(\sqrt{|\Omega_{k0}|}H_0\chi/c)}{(\sqrt{|\Omega_{k0}|}H_0\chi/c)}, & \Omega_{k0} > 0 \quad (\text{Open}). \end{cases} \quad (2.26)$$

This defines the proper radial coordinate r , which is used in all cosmological distance measures.

The angular diameter distance relates an object's physical extent D to its observed angular extent θ on the sky:

$$d_A = \frac{D}{\theta}. \quad (2.27)$$

From the metric, we see that the transverse separation of a source at r subtending an angle $d\theta$ is

$$dD = ar d\theta, \quad (2.28)$$

hence the angular diameter distance:

$$d_A = ar, \quad (2.29)$$

which simplifies to:

$$d_A = a\chi, \quad (2.30)$$

for a flat universe.

Even more relevant for this milestone is the luminosity distance, which is dependent on the measured brightness of standard candles like Type Ia supernovae. We know that the flux F from a source with luminosity L follows an inverse-square law:

$$F = \frac{L}{4\pi d_L^2}. \quad (2.31)$$

In an expanding universe, photons are redshifted and their arrival rate is also affected, leading to the relation:

$$d_L = d_A(1+z)^2 = \frac{d_A}{a^2}. \quad (2.32)$$

This quantity is crucial in observational cosmology as it accounts for both the geometric distance and the redshifted energy of photons. It is therefore fundamental for interpreting supernovae observations and measuring cosmic expansion.

2.1.3. Key cosmological epochs

Though it also has been verified by numerous observations, based on the expression for the Hubble parameter it is not hard to see that the Universe must have gone through phases where its energy budget was (or will be) dominated by radiation, matter and dark energy, separately, in that order. This implies that there must have been a point in time where the Universe was equal amounts of radiation and matter (matter and dark energy), if we neglect the curvature and dark energy (radiation). At radiation-matter equality (rm) we have

$$\Omega_{r,rm} = \Omega_{m,rm} \Leftrightarrow \Omega_{r0}e^{-4x_{rm}} = \Omega_{m0}e^{-3x_{rm}}, \quad (2.33)$$

and thus

$$x_{rm} = \log\left(\frac{\Omega_{r0}}{\Omega_{m0}}\right). \quad (2.34)$$

Using that $x = \log a$ and $z = 1/a - 1$ this gives us an expression for the redshift at rm :

$$z_{rm} = \frac{\Omega_{m0}}{\Omega_{r0}} - 1. \quad (2.35)$$

Similarly, at matter-dark energy equality ($m\Lambda$) we have

$$\Omega_{m0}e^{-3x_{m\Lambda}} = \Omega_{\Lambda0} \Leftrightarrow x_{m\Lambda} = \frac{1}{3} \log\left(\frac{\Omega_{m0}}{\Omega_{\Lambda0}}\right), \quad (2.36)$$

and thus

$$z_{m\Lambda} = \left(\frac{\Omega_{\Lambda0}}{\Omega_{m0}}\right)^{1/3} - 1. \quad (2.37)$$

To ensure that the numerical results presented in this work agree with analytical expectations, it is beneficial to have approximate expressions for the cosmic and conformal times in the different regimes. For a universe dominated by a single component with equation of state w_i the cosmic time t is given by

$$t = \int_0^t dt' = \int_{-\infty}^x \frac{dx'}{H_0 \sqrt{\Omega_{i0}e^{-3(1+w_i)x'}}}. \quad (2.38)$$

When the Universe transitions between an era where its energy density is dominated by some component ρ_j to some other component ρ_i , we may neglect all other components and compute an approximate expression for the cosmic time as function of x by writing

$$t_i(x) \approx t_{j,i} + \int_{x_{j,i}}^x \frac{dx'}{H_0 \sqrt{\Omega_{i0}e^{-3(1+w_i)x'}}}, \quad (2.39)$$

where $x_{j,i}$ and $t_{j,i}$ correspond to their values when $\rho_j = \rho_i$. For radiation we simply have $x_{j,i} = -\infty$ and thus $t_{j,i} = 0$, since the very early Universe was filled with relativistic particles, hence

$$t_r(x) = \int_{-\infty}^x \frac{dx'}{H_0 \sqrt{\Omega_{r0}e^{-4x'}}} = \frac{1}{2H_0 \sqrt{\Omega_{r0}e^{-4x}}}. \quad (2.40)$$

We see that radiation-matter equality occurs at

$$t_{rm} = t_r(x_{rm}) = \frac{\Omega_{r0}^{3/2}}{2H_0\Omega_{m0}^2},$$

and for matter it then follows

$$\begin{aligned} t_m(x) &\approx t_{rm} + \int_{x_{rm}}^x \frac{dx'}{H_0 \sqrt{\Omega_{m0} e^{-3x'}}}, \\ &= \frac{\Omega_{r0}^{3/2}}{2H_0\Omega_{m0}^2} + \frac{2}{3H_0} \left[\frac{1}{\sqrt{\Omega_{m0} e^{-3x}}} - \frac{\Omega_{r0}^{3/2}}{H_0\Omega_{m0}^2} \right], \\ &= \frac{1}{3H_0} \left[\frac{2}{\sqrt{\Omega_{m0} e^{-3x}}} - \frac{\Omega_{r0}^{3/2}}{2\Omega_{m0}^2} \right], \end{aligned} \quad (2.41)$$

with matter-dark energy equality occurring at

$$t_{m\Lambda} = \frac{1}{3H_0} \left[\frac{2}{\sqrt{\Omega_{\Lambda 0}}} - \frac{\Omega_{r0}^{3/2}}{2\Omega_{m0}^2} \right]. \quad (2.42)$$

Lastly, for dark energy we have

$$\begin{aligned} t_\Lambda(x) &\approx t_{m\Lambda} + \int_{x_{m\Lambda}}^x \frac{dx'}{H_0 \sqrt{\Omega_{\Lambda 0}}}, \\ &= \frac{1}{3H_0} \left[\frac{2}{\sqrt{\Omega_{\Lambda 0}}} - \frac{\Omega_{r0}^{3/2}}{2\Omega_{m0}^2} \right] + \frac{1}{H_0 \sqrt{\Omega_{\Lambda 0}}} \left[x - \frac{1}{3} \log \left(\frac{\Omega_{m0}}{\Omega_{\Lambda 0}} \right) \right], \\ &= \frac{1}{H_0 \sqrt{\Omega_{\Lambda 0}}} \left[x + \frac{2}{3} - \frac{1}{3} \log \left(\frac{\Omega_{m0}}{\Omega_{\Lambda 0}} \right) - \frac{\sqrt{\Omega_{\Lambda 0}} \Omega_{r0}^{3/2}}{6\Omega_{m0}^2} \right]. \end{aligned} \quad (2.43)$$

From these derived expressions, it is obvious that $a \propto t^{1/2}$ in the radiation dominated era, $a \propto t^{2/3}$ in the matter era and $a \propto e^{H_0 \sqrt{\Omega_{\Lambda 0}} t}$ in the dark energy era, which is the expected result.

Following an analogous approach for the conformal time, it is straight-forward to show that since

$$\eta_i(x) \approx \eta_{ji} + \int_{x_{ji}}^x \frac{cdx'}{H_0 \sqrt{\Omega_{i0} e^{-(1+3w_i)x'}}}, \quad (2.44)$$

we have the following approximate expressions:

$$\eta_r(x) = \frac{c}{H_0 \sqrt{\Omega_{r0} e^{-2x}}}, \quad (2.45)$$

$$\eta_m(x) = \frac{c}{H_0} \left[\frac{2}{\sqrt{\Omega_{m0} e^{-x}}} - \frac{\sqrt{\Omega_{r0}}}{\Omega_{m0}} \right], \quad (2.46)$$

$$\eta_\Lambda(x) = -\frac{c}{H_0} \left[\frac{1}{\sqrt{\Omega_{\Lambda 0} e^{2x}}} + \frac{\sqrt{\Omega_{r0}}}{\Omega_{m0}} - \frac{3}{\Omega_{m0}^{1/3} \Omega_{\Lambda 0}^{1/6}} \right], \quad (2.47)$$

with the conformal equality times:

$$\eta_{rm} = \frac{c}{H_0} \frac{\sqrt{\Omega_{r0}}}{\Omega_{m0}}, \quad (2.48)$$

$$\eta_{m\Lambda} = \frac{c}{H_0} \left[\frac{2}{\Omega_{m0}^{1/3} \Omega_{\Lambda 0}^{1/6}} - \frac{\sqrt{\Omega_{r0}}}{\Omega_{m0}} \right]. \quad (2.49)$$

To be able to actually test the validity of the approximations made above, it is essential to use them to compute the expected values of some scaled expressions, as this makes it easier to see the relative errors. Obviously, in an era dominated by component i we have

$$\mathcal{H}_i \approx H_0 \sqrt{\Omega_{i0} e^{-(1+3w_i)x}}, \quad (2.50)$$

and in the radiation dominated era we thus have

$$\left(\frac{d\mathcal{H}}{dx} \right)_r = -H_0 \sqrt{\Omega_{r0}} e^{-x} = -\mathcal{H}_r \Leftrightarrow \left(\frac{1}{\mathcal{H}} \frac{d\mathcal{H}}{dx} \right)_r = -1, \quad (2.51)$$

$$\left(\frac{d^2\mathcal{H}}{dx^2} \right)_r = H_0 \sqrt{\Omega_{r0}} e^{-x} = \mathcal{H}_r \Leftrightarrow \left(\frac{1}{\mathcal{H}} \frac{d^2\mathcal{H}}{dx^2} \right)_r = 1. \quad (2.52)$$

Similarly, we have

$$\left(\frac{d\mathcal{H}}{dx} \right)_m = -\frac{\mathcal{H}_m}{2} \Leftrightarrow \left(\frac{1}{\mathcal{H}} \frac{d\mathcal{H}}{dx} \right)_m = -\frac{1}{2}, \quad (2.53)$$

$$\left(\frac{d^2\mathcal{H}}{dx^2} \right)_m = \frac{\mathcal{H}_m}{4} \Leftrightarrow \left(\frac{1}{\mathcal{H}} \frac{d^2\mathcal{H}}{dx^2} \right)_m = \frac{1}{4}. \quad (2.54)$$

in the matter dominated era, and

$$\mathcal{H}_\Lambda = \left(\frac{d\mathcal{H}}{dx} \right)_\Lambda = \left(\frac{d^2\mathcal{H}}{dx^2} \right)_\Lambda = H_0 \sqrt{\Omega_{\Lambda 0}} e^x, \quad (2.55)$$

in the dark energy dominated era. From the latter it is obvious that

$$\left(\frac{1}{\mathcal{H}} \frac{d\mathcal{H}}{dx} \right)_\Lambda = \left(\frac{1}{\mathcal{H}} \frac{d^2\mathcal{H}}{dx^2} \right)_\Lambda = 1. \quad (2.56)$$

maybe move "to ensure..." and down to app.

2.1.4. Onset of acceleration

When analyzing a simulated CMB power spectrum and comparing it to observations, it is interesting to know when the expansion of the Universe started to accelerate. It is a well known fact that the expansion rate (governed by \dot{a}) is increasing as of today, and that we are in the early stage of a dark energy dominated era. We have the second Friedmann equation

$$\frac{\ddot{a}}{a} = -\frac{4\pi G}{3} \sum_i \rho_i (1 + 3w_i), \quad (2.57)$$

where the sum runs over all components (matter, radiation, etc.). The onset of acceleration occurs when \ddot{a} switches sign, i.e., when

$$\sum_i \rho_i (1 + 3w_i) = 0. \quad (2.58)$$

Assuming that this happens well after the radiation dominated era, we can approximate this as

$$\rho_m(x_{\text{acc}}) - 2\rho_\Lambda(x_{\text{acc}}) = 0 \quad (2.59)$$

Using that the expression (2.10) for the density parameters at arbitrary a , we can rewrite eq. (2.60) to get

$$\Omega_{m0} e^{-3x_{\text{acc}}} = 2\Omega_{\Lambda 0} \Leftrightarrow x_{\text{acc}} = \frac{1}{3} \log \left(\frac{\Omega_{m0}}{2\Omega_{\Lambda 0}} \right). \quad (2.60)$$

This corresponds to a redshift

$$z_{\text{acc}} = \left(\frac{2\Omega_{\Lambda 0}}{\Omega_{m0}} \right)^{1/3} - 1. \quad (2.61)$$

Obviously, $t_{\text{acc}} < t_{m\Lambda}$, so we can make the same approximation this time, hence

$$t_{\text{acc}} = t_m(x_{\text{acc}}) = \frac{1}{3H_0} \left[\sqrt{\frac{2}{\Omega_{\Lambda 0}}} - \frac{\Omega_{r0}^{3/2}}{2\Omega_{m0}^2} \right], \quad (2.62)$$

with the conformal time being

$$\eta_{\text{acc}} = \eta_m(x_{\text{acc}}) = \frac{c}{H_0} \left[\frac{2^{5/6}}{\Omega_{m0}^{1/3} \Omega_{\Lambda 0}^{1/6}} - \frac{\sqrt{\Omega_{r0}}}{\Omega_{m0}} \right]. \quad (2.63)$$

rewrite this if appendix

2.1.5. The Universe today

It is of course a great consistency check to see if I am able to replicate the values for the age of the Universe and its horizon size today, and we can use the expressions derived above to do so. Following the approximations I have done up until this point, we have

$$t_0 \approx t_\Lambda(0) = \frac{1}{H_0 \sqrt{\Omega_{\Lambda 0}}} \left[\frac{2}{3} - \frac{1}{3} \log \left(\frac{\Omega_{m0}}{\Omega_{\Lambda 0}} \right) - \frac{\sqrt{\Omega_{\Lambda 0}} \Omega_{r0}^{3/2}}{6 \Omega_{m0}^2} \right], \quad (2.65)$$

$$\eta_0 \approx \eta_\Lambda(0) = -\frac{c}{H_0} \left[\frac{1}{\sqrt{\Omega_{\Lambda 0}}} + \frac{\sqrt{\Omega_{r0}}}{\Omega_{m0}} - \frac{3}{\Omega_{m0}^{1/3} \Omega_{\Lambda 0}^{1/6}} \right]. \quad (2.66)$$

as we know that we currently are in the beginning of a dark energy dominated era.

2.1.6. The χ^2 -method

After having established the theoretical framework describing the evolution of the Universe, we now turn to how observational data can be used to constrain cosmological parameters. One of the most powerful tools for this is the study of Type Ia supernovae, which serve as standard candles for measuring the expansion history of the Universe. Given their intrinsic luminosity, the observed flux allows us to determine their luminosity distance d_L as a function of redshift z , providing a direct probe of the Universe's geometry and expansion.

To quantitatively compare theoretical models to observational data, we define the so-called chi-squared statistic:

$$\chi^2(h, \Omega_{m0}, \Omega_{k0}) = \sum_{i=1}^N \frac{[d_L(z_i, h, \Omega_{m0}, \Omega_{k0}) - d_L^{\text{obs}}(z_i)]^2}{\sigma_i^2}, \quad (2.67)$$

where N is the number of data points, $d_L^{\text{obs}}(z_i)$ represents the measured luminosity distance at redshift z_i , and σ_i is the associated measurement uncertainty. This function quantifies how well a given set of parameters $(h, \Omega_{m0}, \Omega_{k0})$ fits the data: a lower χ^2 value corresponds to a better fit.

2.2. Implementation details

2.2.1. The fiducial model

As mentioned in section 1, I adopt the best-fit Planck 2018 cosmology (see [Planck Collaboration et al. 2020](#)) as my fiducial model, with values chosen within their stated uncertainties. This includes the following parameters:

$$\begin{aligned} h &= 0.67, \\ T_{\text{CMB0}} &= 2.7255 \text{ K}, \\ N_{\text{eff}} &= 3.046, \\ \Omega_{b0} &= 0.05, \\ \Omega_{\text{CDM0}} &= 0.267, \\ \Omega_{k0} &= 0. \end{aligned}$$

Here, h is the dimensionless Hubble constant, which is related to the commonly presented Hubble constant through

$$H_0 = 100h \text{ km s}^{-1} \text{ Mpc}^{-1}. \quad (2.68)$$

The photon and neutrino density parameters are easily calculated using the values for T_{CMB0} and N_{eff} , and since all the density parameters must sum up to unity, we have

$$\begin{aligned} \Omega_{\gamma 0} &= 5.50896 \times 10^{-5}, \\ \Omega_{\nu 0} &= 3.81093 \times 10^{-5}, \\ \Omega_{\Lambda 0} &= 0.683. \end{aligned}$$

2.2.2. Main program structure

As mentioned in section 1, all the code I have used is located on my [GitHub repository](#). In this section I specify which files are relevant for this milestone, and roughly what they contain and how they should be implemented. All of the source codes, which are implemented in C++, are located in the `src` folder, including the main program `Main.cpp`. Naturally, the `scripts` folder contains Python scripts, wherein NumPy and Matplotlib are used for plotting and analyzing the results. The `data` and `results` folders contain data and outputs from the source code, respectively, in the form of `.txt` files, while figures are placed in `figs`. [maybe remove folder info](#)

The evolution of the conformal and cosmic times, Hubble parameter, density parameters and related quantities are computed using the `BackgroundCosmology` class, implemented in `BackgroundCosmology.cpp` and `BackgroundCosmology.h`. Necessary constants and units are defined in their SI-unit values in `Utils.h`, as well as some convenient data types. The fundamental equations governing the expansion are integrated numerically using a GSL-based ODE solver (see `ODESolver.cpp` and `ODESolver.h`). The solutions for $t(x)$ and $\eta(x)$ are stored at discrete values of x and are interpolated using cubic splines (see `Spline.cpp` and `Spline.h`) for efficient lookup, which also ensure smooth evaluations of these quantities at any redshift. This is implemented within the `BackgroundCosmology` class, and all results produced here are written to file and analyzed in `background.py`.

2.2.3. Initial conditions

To numerically solve for conformal time η and cosmic time t , we need appropriate initial conditions. Integrating from $x = -\infty$ (i.e., the Big Bang) is of course impossible, and we may therefore choose an early starting time x_{start} instead, and use the analytical approximations in the radiation-dominated era:

$$\eta(x_{\text{start}}) = \frac{c}{H_0 \sqrt{\Omega_{r0}} e^{-2x_{\text{start}}}} \approx \frac{c}{\mathcal{H}(x_{\text{start}})}, \quad (2.69)$$

$$t(x_{\text{start}}) = \frac{1}{2H_0 \sqrt{\Omega_{r0}} e^{-4x_{\text{start}}}} \approx \frac{1}{2\mathcal{H}(x_{\text{start}})}. \quad (2.70)$$

This ensures a smooth transition between analytical and numerical solutions, minimizing errors when solving for the full evolution of $\eta(x)$ and $t(x)$.

2.2.4. Integration limits and points

When integrating to solve for η and t , I chose to use $x_{\text{min}} = -21.0$ and $x_{\text{max}} = 6.0$ as integration limits, with $n = 1000$ points. However, when splining the results I used $x_{\text{min}} = -20.0$ and $x_{\text{max}} = 5.0$ instead, so as to not include the likely more unstable endpoints, with $n = 2501$ points (corresponding to $\Delta x = 0.01$) for smoother visualization.

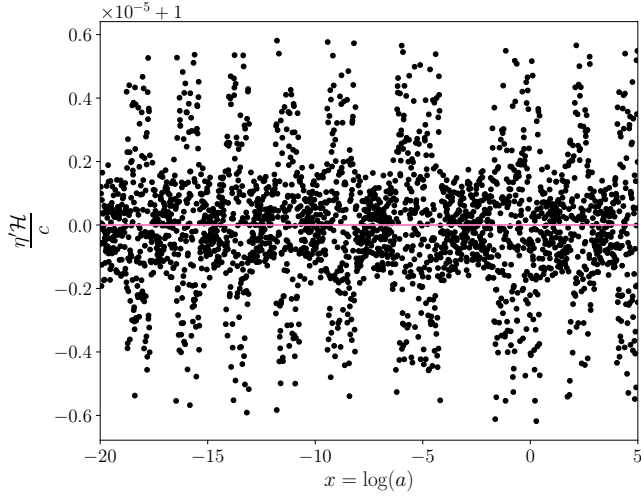


Fig. 2.1. Comparison of the numerically computed conformal time derivative $\eta'H/c$ with the expected value of 1 (pink line). The small deviations on the order of $\lesssim 10^{-5}$ confirm the numerical stability of the integration.

2.2.5. Supernova fitting

To constrain cosmological parameters ($h, \Omega_{m0}, \Omega_{k0}$), I performed a Markov Chain Monte Carlo (MCMC) fit to Type Ia supernova data (see `supernovadata.txt`), which is implemented in `SupernovaFitting.h`. The MCMC chain consists of 10 000 samples, where I have treated the 200 first samples as burn-in time and thus discarded them. The results are further analyzed in `supernova.py`, where I visualize the accepted samples within the $(\chi^2 - \chi^2_{\min}) < 1\sigma$ and $(\chi^2 - \chi^2_{\min}) < 2\sigma$, constraints in the $(\Omega_{m0}, \Omega_{\Lambda0})$ -plane, corresponding to 68.3% and 95.45% confidence levels, respectively. I use tabulated values of $1\sigma = 3.53$ and $2\sigma = 8.02$ (see [Reid Accessed: February 2025](#)), since we have $k = 3$ degrees of freedom. This is because we really have four parameters ($h, \Omega_{m0}, \Omega_{k0}, \Omega_{\Lambda0}$), but also the constraint that all the density parameters must sum up to unity, which eliminates one d.o.f.

2.2.6. Testing numerical stability

To test the stability of the numerical solutions presented in the following section, I have plotted $\eta'H/c$ as function of x in figure 2.1, since this quantity should remain close to unity throughout the range. The scatter points, which were obtained by taking the derivative of the spline for η , show small deviations from 1, on the order of $\lesssim 10^{-5}$, indicating that the numerical error is very small. It also remains bounded throughout the range of x , suggesting that the ODE solver maintains stability and does not accumulate significant numerical drift. The slight periodic variations could result from finite step sizes in the integration, or have something to do with interpolation errors between the integration points, but they are well within an acceptable tolerance.

TODO: maybe move over prev. sec.

2.3. Results and discussions

2.3.1. The conformal Hubble parameter

In figure 2.2 I have plotted the exact evolution of the conformal Hubble parameter $\mathcal{H}(x)$ (black solid line), with approximations in the different cosmological epochs overplotted (dashed lines).

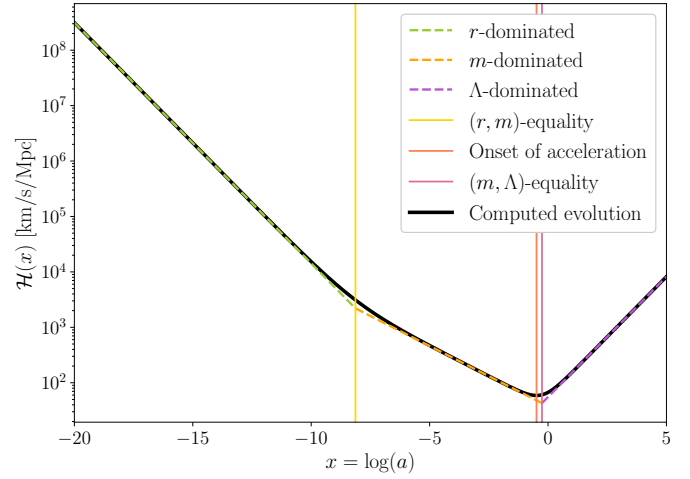


Fig. 2.2. Exact evolution of the conformal Hubble parameter $\mathcal{H}(x)$ (black) compared with approximations (dashed). The onset of acceleration is visible as a departure from matter-like scaling, occurring at the trough of the exact solution.

Green, orange and purple correspond to radiation-, matter- and dark energy-dominated eras, respectively, with the yellow, red and pink vertical lines marking radiation-matter equality, onset of acceleration, and matter-dark energy equality. We see that the approximations closely follow the exact solution, staying at the correct order of magnitude at all times, although the deviations are significant close to the equality times. These are of course to be expected, since the approximations were derived under the assumption of the Universe only containing the dominating component within the different eras, which of course is not realistic as we transition from one to another. Thus, the result is still a great validation for the approximations, which indicates that we can safely use them to verify the numerical solutions for η and t .

A more direct comparison between the approximations and the exact evolution can be seen in figure 2.3, where I have plotted the first (left) and second (right) derivatives of \mathcal{H} with respect to x , divided by \mathcal{H} to see relative differences more easily. The dashed lines of different colors represent the same things here as well. We see good agreement in the asymptotically radiation-dominated and dark energy-dominated regimes, while in the matter-dominated epoch and around the equality times there are clear deviations, especially for the double derivative. This is reasonable, as we make rough approximations in both the beginning and the end of this era, hence the exact solution barely has time to sink to the expected value before it rises at the next transition point.

It is interesting to see that the scaled double derivative actually increases beyond the expected value in the beginning of the dark energy-dominated era, with the peak being today. To understand this, we can look back at eqs. (2.17) and (2.18). The latter shows that the second derivative is influenced by a competition between growing and decaying terms as the Universe evolves: During the matter-dominated era, the dominant term is $\Omega_{m0}e^{-x}$, which leads to a slow decrease in \mathcal{H} ; as Λ begins to dominate, the exponential growth of the $2\Omega_{\Lambda0}e^{2x}$ term starts accelerating the Universe. The transition is not instantaneous, meaning there is a period where the competing effects of matter dilution (e^{-x}) and dark energy growth (e^{2x}) cause a rapid shift in dynamics. This is visible in the sharp turn of \mathcal{H} in figure 2.2, and explains

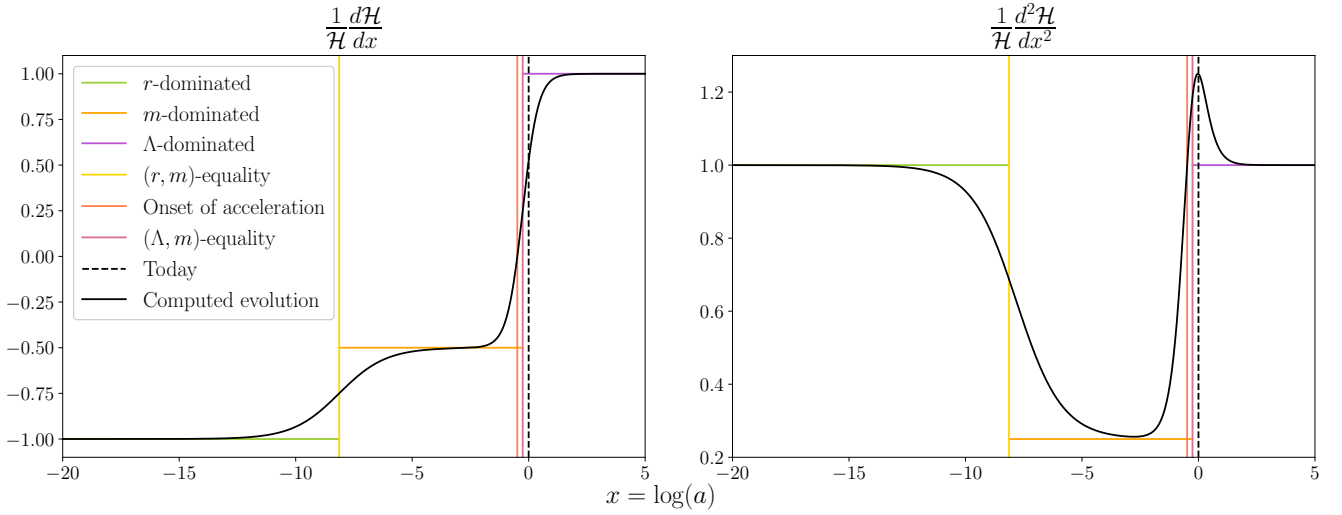


Fig. 2.3. Comparison of exact evolutions (black) with approximations (dashed) for the scaled first and second derivatives of $\mathcal{H}(x)$. Agreement is good in pure radiation and matter domination but deviates near transitions due to neglected components.

the peak in the scaled second derivative before it settles into the Λ -dominated regime.

2.3.2. Time and horizon measures

In figure 2.4 I have plotted the numerical solutions for the conformal time η/c (grey) and the cosmic time t (black) as functions of x , with the approximate analytical solutions presented in section 2.1 overplotted with dashed lines. The two bottom subplots, where the cosmic time is in focus, are included to easily be able to study what happens where the discrepancies between the numerical and analytical solutions are most drastic: where the Universe transitions from being dominated by one component to another. As expected, we see that the analytical approximation starts to deviate from the numerical curve as we approach (r, m) -equality, and eventually meets it again after. This happens also for the (m, Λ) -equality, but here the deviation actually continues to grow before it falls down again.

In table 2.1 I have listed key cosmological timestamps for important transition points in the Universe's history: radiation-matter equality, the onset of acceleration, matter-dark energy equality, and present-day values. The logarithmic scale factor $x = \log a$ and redshift z are listed for each event, along with analytical and numerical results for cosmic time t , conformal time η/c , and the comoving horizon η . We observe a discrepancy between the analytically approximated values for t and η obtained using the expressions derived in section 2.1 and the corresponding numerical values, which instead were obtained by solving the full system of equations and interpolating via splines. These discrepancies are consistent with figure 2.4.

compare r-m eq w/ Planck!

In Planck Collaboration et al. (2020), one presented estimate of the age of the Universe is $t_0 = 13.801 \pm 0.024$ Gyr. This is based on 1σ constraints on a combination of gravitational lensing and TT (temperature), TE (temperature-E mode polarization), EE (E mode polarization) and lowE (low multipole E-mode polarization) angular power spectra measurements. This is in good agreement with the numerical result, although the value stated here is slightly larger. Nevertheless, the analytical approximation greatly overestimate it in comparison. This further validates the numerical solution around the equality times, where

it deviates from the approximate evolutions and we have less to compare it to.

2.3.3. Density parameters

The evolutions of the density parameters $\Omega_i(x)$ are plotted in figure 2.5, with solid lines for Ω_r , Ω_m and Ω_Λ , and dashed lines for the individual components that make up the two first of these. The solid curves are consistent with the previous results, with the transitions between the different eras matching the observed changes in \mathcal{H} , η and t . For example, the abrupt change in the conformal Hubble parameter at (m, Λ) -equality compared to the change at (r, m) -equality matches the relatively rapid takeover of Λ as the dominating energy component, as opposed to the more gradual change from radiation to matter domination.

2.3.4. Supernova fitting

When running the MCMC fits, the minimum chi-squared value obtained was $\chi^2_{\min} = 29.2867$, corresponding to the parameter values listed in the third column of table 2.2. The means μ_i and standard deviations σ_i (where i runs over the parameters) computed for the samples within the 1σ constraints are listed as well, in addition to the Planck parameters stated in Planck Collaboration et al. (2020) for comparison. Interestingly, the supernova measurements favor a slightly open universe, deviating from the Planck result of a flat universe. However, the standard deviation, which is about three times larger than the best-fit value, suggests that the data does not strongly constrain curvature. We also see that the Planck result for Ω_{m0} is higher than the best-fit value, though it is within the $1\sigma_m$ confidence interval.

After obtaining the best-fit values I made a new instance of BackgroundCosmology with these parameters and solved for this universe as well. In figure 2.6 I have plotted the scaled luminosity distance d_L/z against z for this best-fit cosmology (black curve) as well as the Planck cosmology (grey curve), together with the data points d_L^{obs}/z with scaled errorbars (pink). We see that the best-fit cosmology aligns much better with the data points than the Planck model, as the latter does not always lie within the supernova errorbars. This reflects the fact that the Planck data prefers a flat universe, whereas the best-fit suggests

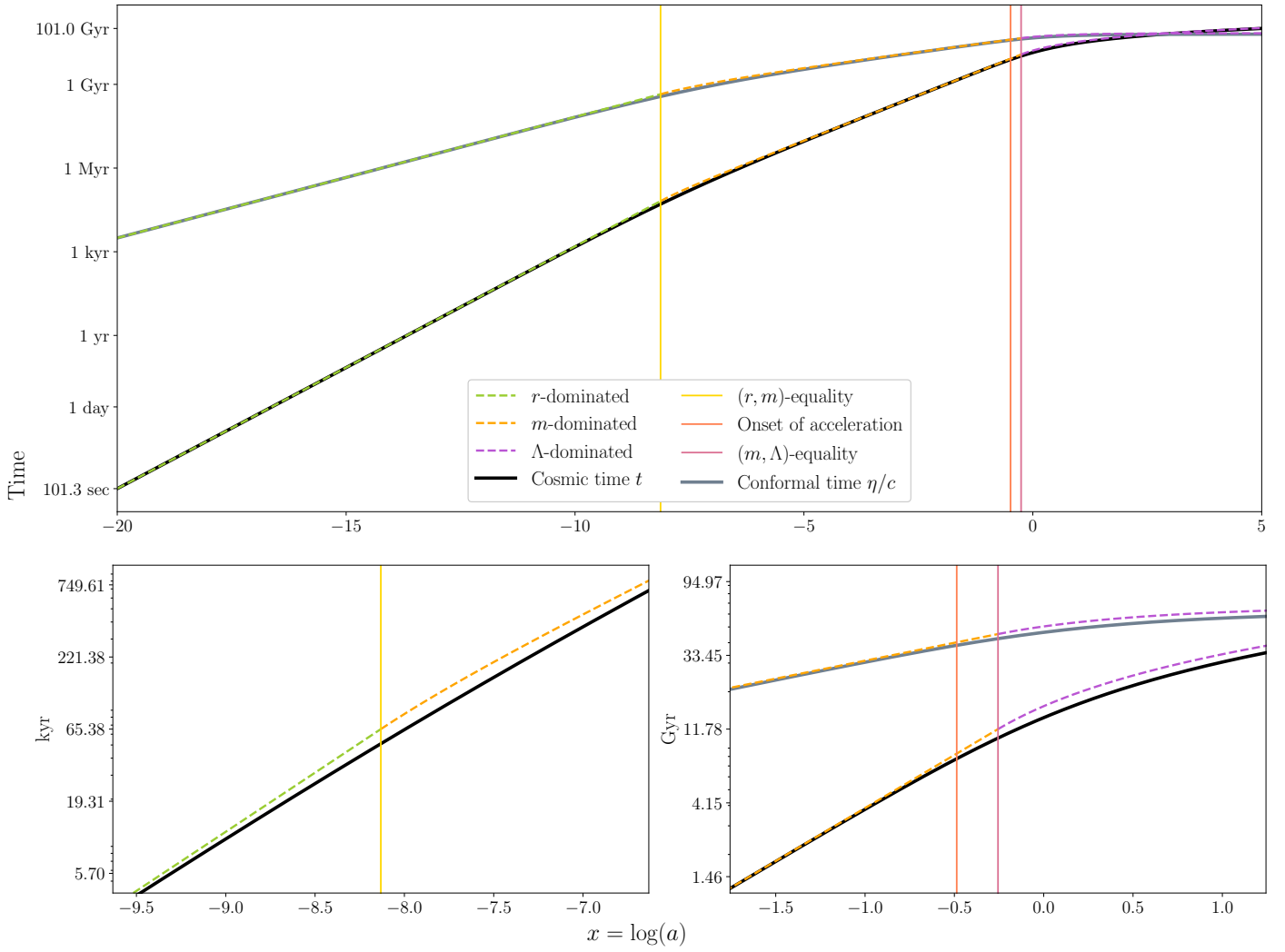


Fig. 2.4. Conformal time $\eta(x)$ (grey) and cosmic time $t(x)$ (black) compared with analytical approximations (dashed). Deviations near equality points arise due to gradual transitions between dominant energy components. This is highlighted in the bottom subplots for the cosmic time.

Table 2.1. Key cosmological timestamps at radiation-matter equality, the onset of acceleration, matter-dark energy equality, and present-day values. The analytical values are obtained using approximations from the theory section, while the numerical values are extracted from splines after solving the full system of equations. Discrepancies between the two highlight the limitations of the analytical approximations, especially during transition epochs.

| | Radiation-matter equality | Onset of acceleration | Matter-dark energy equality | Present day values |
|-----------------------|---------------------------|-----------------------|-----------------------------|--------------------|
| x | -8.13 | -0.49 | -0.26 | 0 |
| z | 3400.33 | 0.63 | 0.29 | 0 |
| t (analytical) | 65.38 kyr | 8.33 Gyr | 11.78 Gyr | 16.30 Gyr |
| t (numerical) | 51.06 kyr | 7.75 Gyr | 10.38 Gyr | 13.86 Gyr |
| η/c (analytical) | 444.75 Myr | 40.22 Gyr | 45.20 Gyr | 50.36 Gyr |
| η/c (numerical) | 368.44 Myr | 38.57 Gyr | 42.37 Gyr | 46.32 Gyr |
| η (analytical) | 136.27 Mpc | 12.32 Gpc | 13.85 Gpc | 15.43 Gpc |
| η (numerical) | 112.89 Mpc | 11.82 Gpc | 12.98 Gpc | 14.19 Gpc |

slightly negative curvature, which alters the distance-redshift relation. It also highlights tensions between low-redshift and high-redshift cosmological probes (see e.g. [Reiss et al. \(2024\)](#) for a recent discussion of this so-called Hubble tension in light of JWST observations). However, it should be kept in mind that measurements of supernova magnitudes can be affected by calibration

uncertainties, host galaxy effects and dust extinction, potentially shifting best-fit cosmological parameters. Nevertheless, the discrepancies underscore the importance of using multiple probes and datasets to break parameter degeneracies and obtain a more complete picture of cosmic expansion.

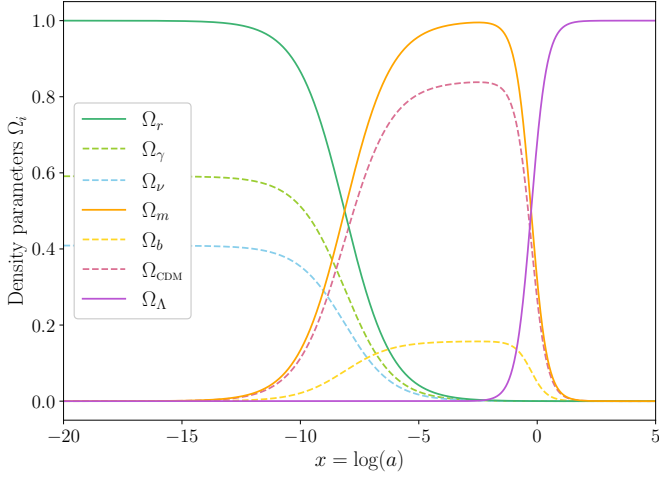


Fig. 2.5. The fractional energy densities of radiation, matter, and dark energy as functions of x (solid lines). The dashed lines show the evolutions of the radiation components (photons and neutrinos) and matter components (baryons and dark matter).

Table 2.2. Best-fit cosmological parameters obtained from supernova data, along with their mean values and standard deviations. The best-fit values correspond to the minimum χ^2 , while the Planck 2018 values estimated from 1σ constraints on TT,TE,EE+lowE+lensing measurements are provided for comparison. These were determined by assuming a perfectly flat Universe, though they do actually estimate a small non-zero curvature density ($\Omega_{k0} = 0.0007 \pm 0.0019$) when relaxing this assumption and also including BAO measurements. I have chosen to neglect this in my analysis, due to the relatively small value and large uncertainty. move to main text? Moreover, the Hubble constant is given in units of km/s/Mpc.

| | μ_i | σ_i | $\min(\chi^2)$ | Planck |
|----------------------|---------|------------|----------------|-------------------|
| H_0 | 70.1 | 0.5 | 70.2 | 67.4 ± 0.5 |
| Ω_{m0} | 0.240 | 0.087 | 0.258 | 0.315 ± 0.007 |
| Ω_{k0} | 0.12 | 0.22 | 0.07 | 0 |
| $\Omega_{\Lambda 0}$ | 0.642 | 0.133 | 0.672 | 0.685 ± 0.007 |

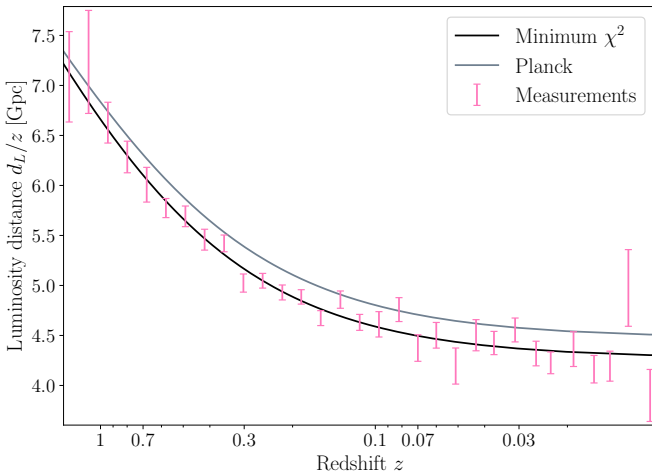


Fig. 2.6. Comparison of the luminosity distances d_L^{obs}/z gathered from supernova observations (pink with errorbars) with the fiducial Planck model (grey) and the best-fit model from MCMC analysis (black).

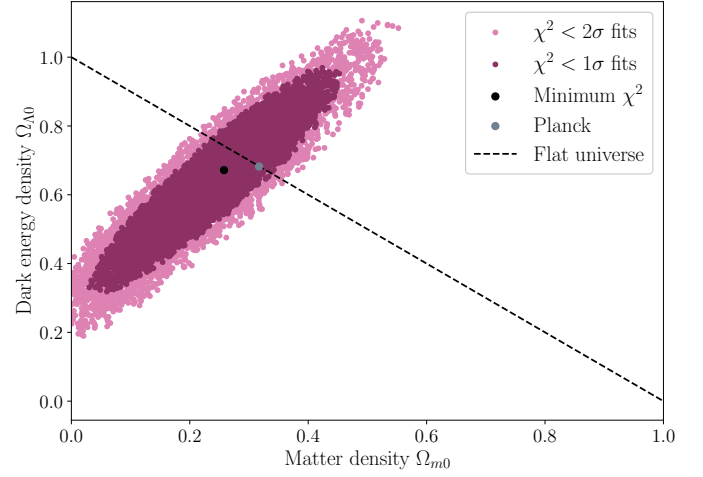


Fig. 2.7. Confidence contours in the $(\Omega_{m0}, \Omega_{\Lambda 0})$ parameter space from the supernova MCMC analysis, compared to the Planck fiducial model. The supernova constraints allow for a slightly open universe, while Planck favors flatness based on multi-probe data.

In figure 2.7 I have scatter plotted the accepted $(\Omega_{m0}, \Omega_{\Lambda 0})$ samples within the 1σ and 2σ constraints, with the black (grey) data point showing the best-fit (Planck) parameter set, and the dashed line showing the combinations that allow for a flat universe. We see clearly here that supernova-only constraints allow for slightly different cosmologies than the Planck model, with a preference for a lower matter density and small negative curvature. The Planck data includes additional information from the early universe, leading to a tighter preference for a flat universe with more mass. This discrepancy ties directly to the luminosity distance plot, confirming that these best-fit supernova parameters slightly differ from Planck's and further highlighting the importance of combining multiple datasets for robust cosmological constraints.

Figure 2.8 shows normalized histograms of the samples within the 1σ constraint, with Gaussian fits made with the μ_i and σ_i overplotted to represent the posterior distributions. Most noticeable is how different the supernova and Planck results are for H_0 , with the smallest accepted 1σ samples being as large as 69 km/s/Mpc. Planck's estimate is derived from early universe physics (CMB, baryon acoustic oscillations and large-scale structure), while supernova constraints come from low-redshift expansion. The discrepancy may therefore indicate new and/or unknown physics present at some eras of the expansion history (see Reiss et al. (2024), but also Cort  s & Liddle (2024) for critical discussions on tensions as indicators of new physics), or possibly systematic errors in one or both datasets. Moreover, we see that the supernova-only constraint clearly prefers a lower matter density compared than the Planck estimate, consistent with the MCMC contour plot.

The posterior distribution suggests a preference for a slightly open universe, though with considerable uncertainty. This deviation from flatness may arise because supernovae alone do not tightly constrain curvature, as they primarily measure relative distances, not absolute spatial curvature. Moreover, we see that the histograms are not perfectly Gaussian, particularly those for Ω_{m0} and Ω_{k0} . Specifically, the asymmetry with more samples in the low mass/negative curvature ends may suggest a skewed uncertainty, indicating that a simple Gaussian error estimate might underestimate the possible range of accepted values.

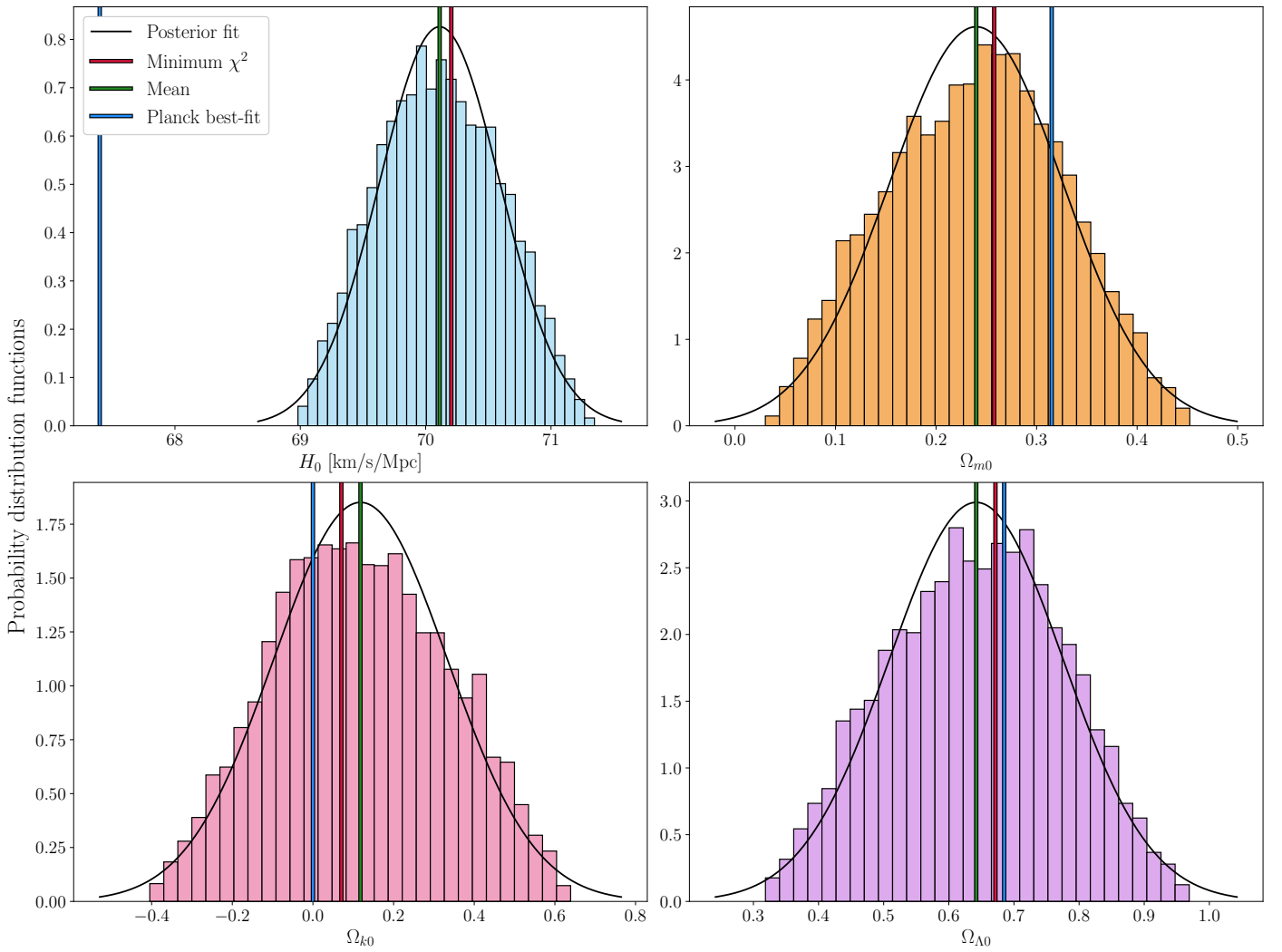


Fig. 2.8. Histograms of the MCMC posterior distributions for the parameters (H_0 , Ω_{m0} , Ω_{k0} , $\Omega_{\Lambda 0}$), compared with Gaussian fits (solid curves) and Planck values. Deviations from Gaussianity indicate asymmetries in parameter uncertainties.

maybe remove/argue for good in ast. standards

3. Milestone II: Recombination History

In the previous milestone, I established a numerical framework for solving the background evolution of the Universe, validating the results against analytical approximations and observational constraints. This provided a foundation for understanding the expansion history and cosmic distances, key ingredients in interpreting cosmological data. However, to model the formation of the CMB and its anisotropies, we must now extend the analysis to include recombination history: the period when the Universe transitioned from an ionized plasma to a neutral state, allowing photons to decouple from matter. This process determines the surface of last scattering, setting the initial conditions for the CMB fluctuations we observe today.

In this milestone, I compute the recombination and reionization history by solving the Saha and Peebles equations, track the evolution of the optical depth $\tau(x)$, and derive the visibility function $\tilde{g}(x)$, which quantifies when CMB photons last interacted with free electrons. These quantities are essential for accurately modeling the temperature and polarization anisotropies of the CMB in the next milestones. Additionally, I compute the sound horizon at decoupling, a fundamental scale imprinted in

the CMB power spectrum. This milestone bridges the gap between background cosmology and perturbation theory, ensuring that my model of the early Universe correctly captures the physics governing photon-matter interactions before recombination. maybe change/shorten

3.1. Theoretical framework

3.1.1. The Boltzmann equation and interactions

In cosmology, the evolution of particle species is governed by their phase-space distribution function, which in thermal equilibrium takes the following form:

$$f(E) = \frac{1}{e^{(E-\mu)/T} \pm 1}. \quad (3.1)$$

Here, E is the energy of the particle, μ is the chemical potential, and T is the temperature of the system. The plus sign corresponds to the Fermi-Dirac distribution, and the minus sign to the Bose-Einstein distribution, which apply to fermions and bosons, respectively. For non-relativistic particles ($E \gg T$), the exponential terms in the denominator dominate, leading to the classical Maxwell-Boltzmann distribution:

$$f(E) \approx e^{-(E-\mu)/T}. \quad (3.2)$$

This approximation is valid for massive species that are thermally decoupled or at sufficiently low temperatures. It plays a crucial role in describing the abundance of baryons and cold dark matter in the late Universe.

The phase-space distribution functions serve as the foundation for the Boltzmann equation, which governs the evolution of number densities, energy densities, and momenta of different species as the Universe expands. In general relativity, the Boltzmann equation can be written as an equation in terms of an affine parameter λ :

$$\frac{df}{d\lambda} = C[f], \quad (3.3)$$

Here, $C[f]$ is the collision term, which is generally obtained from quantum field theory and encodes interactions between particles. In a homogeneous and isotropic universe, it vanishes when species are in thermal equilibrium, as detailed balance ensures that the rate of interactions maintains the equilibrium distribution.

In cosmology, we primarily consider $1 + 2 \rightleftharpoons 3 + 4$ interactions, where the most crucial to consider are Compton scattering of photons off electrons, Coulomb scattering of electrons off protons, and Hydrogen recombination and ionization:

$$e^- + \gamma \rightleftharpoons e^- + \gamma, \quad (3.4)$$

$$e^- + p \rightleftharpoons e^- + p, \quad (3.5)$$

$$e^- + p \rightleftharpoons H + \gamma. \quad (3.6)$$

The most relevant interaction for computing the CMB is Compton scattering in its low-energy (Thomson) limit, as this governs the coupling between electrons and photons in the early Universe. It is thus crucial for the optical depth, a quantity I introduce in section 3.1.6 that will prove to be essential as we move on to perturbations. Moreover, Coulomb scattering is only indirectly important, as its strength ensures that we can treat electrons and protons as a single particle species (baryons). Lastly, Hydrogen (as well as Helium) recombination and ionization is crucial for the recombination history. This is studied more in detail in sections 3.1.3 through 3.1.5.

3.1.2. Mass fractions

Rather than tracking the absolute number densities of different particle species, it is convenient to define mass fractions to describe relative species abundances. The most important of these is the free electron fraction, defined as

$$X_e = \frac{n_e}{n_H}, \quad (3.7)$$

where n_e is the number density of free electrons and n_H is the number density of Hydrogen nuclei (both ionized and neutral).

Since Helium is also present in the early Universe, we define the primordial Helium mass fraction Y_p , which represents the fraction of baryonic mass in Helium:

$$Y_p = \frac{m_{\text{He}} n_{\text{He}}}{m_b n_b} = \frac{4n_{\text{He}}}{n_b}, \quad (3.8)$$

where n_{He} is the number density of Helium nuclei and

$$n_b \approx \frac{\rho_b}{m_H} = \frac{\Omega_b \rho_{c0}}{m_H a^3}, \quad (3.9)$$

is the total baryon number density. The factor of 4 in eq. (3.8) accounts for the fact that Helium nuclei (Helium-4) have four

nucleons each. The number density of Hydrogen can easily be expressed in terms of Y_p , as all other elements are negligible for our purposes:

$$n_H = n_b - 4n_{\text{He}} = (1 - Y_p)n_b. \quad (3.10)$$

To fully describe the ionization state of the Universe, it is also necessary to introduce the ionization fractions of Hydrogen and Helium:

$$x_{H+} = \frac{n_{H^+}}{n_H}, \quad (3.11)$$

$$x_{\text{He}+} = \frac{n_{\text{He}^+}}{n_{\text{He}}}, \quad (3.12)$$

$$x_{\text{He}++} = \frac{n_{\text{He}^{++}}}{n_{\text{He}}}. \quad (3.13)$$

Here, x_{H+} represents the fraction of ionized Hydrogen, while $x_{\text{He}+}$ and $x_{\text{He}++}$ describe singly and doubly ionized Helium, respectively. These mass fractions allow for efficient tracking of the recombination process. When including Helium, the free electron number density is given by

$$n_e = 2n_{\text{He}++} + n_{\text{He}+} + n_{H+}, \quad (3.14)$$

which can be rewritten as

$$\frac{n_e}{n_b} = (2x_{\text{He}++} + x_{\text{He}+}) \frac{Y_p}{4} + x_{H+}(1 - Y_p) \equiv f_e. \quad (3.15)$$

The free electron fraction is related to this by:

$$X_e = \frac{f_e}{1 - Y_p}. \quad (3.16)$$

3.1.3. The Saha approximation

To determine how recombination proceeds, we need to quantify the balance between ionization and recombination processes in the early Universe. The evolution of number densities is governed by the Boltzmann equation, and for a general interaction of the type $1 + 2 \rightleftharpoons 3 + 4$ it can be shown that this takes the following form:

$$\frac{1}{a^3} \frac{d(n_1 a^3)}{dt} = -\alpha n_1 n_2 + \beta n_3 n_4. \quad (3.17)$$

Here, $\alpha = \langle \sigma v \rangle$ is the thermally averaged cross-section for the interaction, while β is related to α through equilibrium conditions:

$$\beta = \alpha \left(\frac{n_1 n_2}{n_3 n_4} \right)_{\text{eq}}. \quad (3.18)$$

If equilibrium holds, the right-hand side must vanish, and we obtain an equation relating the equilibrium number densities.

The Saha equation provides an analytical expression for the ionization fraction in equilibrium, valid when the ionization and recombination rates are fast compared to the Hubble expansion rate. It follows from writing eq. (3.18) for the process specified in eq. (3.6) in terms of the free electron fraction X_e . However, in order to derive it we need the number density of a species in thermal equilibrium, which follows from the Maxwell-Boltzmann distribution (eq. (3.2)): **derive this?**

$$n_i = g_i \left(\frac{m_i k_B T}{2\pi \hbar^2} \right)^{3/2} e^{-\epsilon_i/k_B T}, \quad (3.19)$$

where g_i is the statistical degeneracy, m_i is the mass, and ϵ_i is the ionization energy. Using this, we obtain the standard Saha equation for Hydrogen recombination when ignoring Helium altogether: [show more intermediate steps?](#)

$$\frac{X_e^2}{1 - X_e} = \frac{1}{n_H} \left(\frac{m_e k_B T}{2\pi\hbar^2} \right)^{3/2} e^{-\epsilon_0/k_B T}. \quad (3.20)$$

Here, $\epsilon_0 = 13.6$ eV is the ionization energy of Hydrogen. This equation determines how the free electron fraction evolves with temperature, and is an excellent approximation when $X_e \approx 1$.

To compute the recombination history more accurately, we must account for Helium. Conveniently, the ionization history of Helium follows the same principles as for Hydrogen, [should the interactions be specified?](#) and using the ionization fractions defined in section 3.1.2 we obtain three coupled Saha equations for Hydrogen and Helium recombination:

$$n_e \frac{x_{\text{He}+}}{1 - x_{\text{He}+} - x_{\text{He}++}} = 2 \left(\frac{m_e k_B T_b}{2\pi\hbar^2} \right)^{3/2} e^{-\chi_0/k_B T_b}, \quad (3.21)$$

$$n_e \frac{x_{\text{He}++}}{x_{\text{He}+}} = 4 \left(\frac{m_e k_B T_b}{2\pi\hbar^2} \right)^{3/2} e^{-\chi_1/k_B T_b}, \quad (3.22)$$

$$n_e \frac{x_{\text{H}+}}{1 - x_{\text{H}+}} = \left(\frac{m_e k_B T_b}{2\pi\hbar^2} \right)^{3/2} e^{-\epsilon_0/k_B T_b}. \quad (3.23)$$

Here, $\chi_0 = 24.5874$ eV is the ionization energy of neutral Helium, and $\chi_1 = 4\epsilon_0 = 54.42279$ eV is the ionization energy of singly ionized Helium.

Unlike Hydrogen recombination, which can be solved directly using the Saha equation, Helium recombination requires an iterative approach. Given an initial guess for $f_e \approx 1$, we may solve the three Saha equations algebraically for $x_{\text{He}++}$, $x_{\text{He}+}$ and $x_{\text{H}+}$, then compute the corresponding value of f_e using eq. (3.15). This process should be repeated a few times, using the updated f_e as input for the next iteration, until convergence according to some threshold value is reached:

$$|f_e - f_{e,\text{old}}| < \Delta f_{e,\text{tol}}. \quad (3.24)$$

This ensures an accurate determination of the free electron fraction.

3.1.4. The Peebles equation

The Saha approximation provides an accurate description of recombination in the early stages when the ionization and recombination processes are in thermal equilibrium. However, as the universe expands and cools, the recombination rate slows down relative to the Hubble expansion, preventing the free electron fraction X_e from immediately following the equilibrium prediction. To accurately model recombination at later times, when X_e is no longer very close to 1, we must instead use the Peebles equation, which describes the evolution of X_e in an out-of-equilibrium setting. This looks the same whether Helium is included or not, and is given by

$$\frac{dX_e}{dx} = \frac{C_r(T_b)}{H} [\beta(T_b)(1 - X_e) - n_H \alpha^{(2)}(T_b) X_e^2]. \quad (3.25)$$

Most of the quantities that appear in eq. (3.25) are derived from quantum field theory calculations, and I will simply state them and what they represent. First of all,

$$\alpha^{(2)}(T_b) = \frac{64\pi}{\sqrt{27}\pi} \left(\frac{\alpha}{m_e \hbar} \right)^2 \sqrt{\frac{\epsilon_0}{k_B T_b}} \phi_2(T_b), \quad (3.26)$$

and

$$\alpha = \frac{m_e c}{\hbar} \sqrt{\frac{3\sigma_T}{8\pi}} \approx \frac{1}{137.0359992}, \quad (3.27)$$

are the effective recombination coefficient [correct?](#) and the fine-structure constant, respectively, with σ_T being the cross-section for Thomson scattering, and the dimensionless function

$$\phi_2(T_b) = 0.448 \ln \left(\frac{\epsilon_0}{k_B T_b} \right). \quad (3.28)$$

Furthermore,

$$\beta(T_b) = \alpha^{(2)}(T_b) \left(\frac{m_e k_B T_b}{2\pi\hbar^2} \right)^{3/2} e^{-\epsilon_0/k_B T_b}, \quad (3.29)$$

is the recombination rate per unit volume [correct?](#), and

$$C_r = \frac{\Lambda_{2s \rightarrow 1s} + \Lambda_\alpha}{\Lambda_{2s \rightarrow 1s} + \Lambda_\alpha + \beta^{(2)}(T_b)}, \quad (3.30)$$

is the Peebles correction factor, which accounts for the fact that some recombinations result in excited Hydrogen states instead of directly producing neutral Hydrogen. In this expression, $\Lambda_{2s \rightarrow 1s} = 8.227 \text{ s}^{-1}$ is the spontaneous two-photon decay rate of the Hydrogen $2s$ state, and

$$\Lambda_\alpha = \frac{H}{(8\pi)^2 n_{1s}} \left(\frac{3\epsilon_0 \hbar}{c} \right)^3, \quad (3.31)$$

is the Ly- α escape rate, which accounts for the fact that Ly- α photons can redshift out of resonance before being reabsorbed.

[correct?](#) Furthermore,

$$n_{1s} = (1 - X_e) n_H, \quad (3.32)$$

is the number density of Hydrogen in the ground state, and

$$\beta^{(2)}(T_b) = \beta(T_b) e^{3\epsilon_0/4k_B T_b}, \quad (3.33)$$

is the modified recombination rate, which incorporates corrections to $\beta(T_b)$ due to excited Hydrogen states. [correct?](#)

3.1.5. Reionization

Although reionization was likely a complex and extended process, it can be accurately modeled using a simple hyperbolic tangent (tanh) function, as implemented in CAMB (Code for Anisotropies in the Microwave Background, see [Lewis et al. \(2000\)](#)). This approach provides a smooth transition of the free electron fraction X_e from its post-recombination value to a fully ionized state. The modified evolution of the free electron fraction is then given by:

$$X_e = X_e^{\text{Peebles}} + \frac{1 + f_{\text{He}}}{2} \left(1 + \tanh \frac{y_{\text{reion}} - y}{\Delta y_{\text{reion}}} \right), \quad (3.34)$$

where we define $y = (1 + z)^{3/2} = e^{-3x/2}$, and thus $y_{\text{reion}} = (1 + z_{\text{reion}})^{3/2}$ and $\Delta y_{\text{reion}} = \frac{3}{2} \sqrt{1 + z_{\text{reion}}} \Delta z_{\text{reion}}$. Here, z_{reion} is the redshift at which reionization is centered, and Δz_{reion} determines how quickly the transition occurs. These parameters are constrained by CMB data, particularly the large-scale E-mode polarization spectrum.

In eq. (3.34),

$$f_{\text{He}} = \frac{Y_p}{4(1 - Y_p)} \quad (3.35)$$

accounts for the contribution to the reionization process from singly and doubly ionized Helium. The former is assumed to contribute around the same time as Hydrogen reionization, hence the factor $(1 + f_{\text{He}})/2$. Furthermore, Helium likely underwent a second phase of reionization at later times, and this can be modelled by adding a second term:

$$\frac{f_{\text{He}}}{2} \left(1 + \tanh \frac{z_{\text{He, reion}} - z}{\Delta z_{\text{He, reion}}} \right). \quad (3.36)$$

Analogous to the primary reionization process, the parameters that determine the mid-point and duration of this second phase are $z_{\text{He, reion}}$ and $\Delta z_{\text{He, reion}}$, respectively. Though the contribution from Helium is not as crucial as that from Hydrogen, it is still essential to include if one wants to accurately model the thermal history of the Universe.

3.1.6. Optical depths and visibility functions

To understand how photons interact with matter during recombination, we need to study the optical depth, which quantifies the probability of a photon scattering as it travels through the Universe. It is a dimensionless quantity that describes the attenuation of intensity due to scattering. If a source emits radiation with an initial intensity I_0 , then the observed intensity after traveling a distance x through a medium with optical depth τ is given by

$$I(x) = I_0 e^{-\tau(x)}. \quad (3.37)$$

If $\tau \gg 1$ we say that the medium is optically thick, meaning photons scatter many times before escaping. If $\tau \ll 1$ the medium is optically thin, allowing most photons to pass through unimpeded. It is common in cosmology to define $\tau = 1$ as the point of last scattering, where photons transition from being tightly coupled to propagating freely.

As mentioned in section 3.1.1, the primary source of opacity in the early Universe is Thomson scattering of photons off free electrons. Thus, the optical depth of photons at a given conformal time η is defined as the integrated Thomson scattering rate along the line of sight: **correct to say this?**

$$\tau(\eta) = \int_{\eta}^{\eta_0} n_e \sigma_T a d\eta'. \quad (3.38)$$

However, it is more conveniently written on differential form in terms of the chosen time variable x instead: **derive this?**

$$\tau'(x) = \frac{d\tau}{dx} = -\frac{cn_e \sigma_T}{H}, \quad (3.39)$$

which can easily be integrated numerically and splined so that we can compute $\tau(x)$. The second derivative of the optical depth, τ'' , is also useful to compute from this, since it helps characterize the sharpness of changes in τ during important events in the thermal history, such as decoupling and reionization.

A related, but less critical quantity is the baryon optical depth, which quantifies the drag exerted on baryons due to interactions with photons. On differential form it is given by:

$$\tau'_b(x) = \frac{d\tau_b}{dx} = -\frac{cRn_e \sigma_T}{H} = R \frac{d\tau}{dx}, \quad (3.40)$$

where the ratio

$$R(x) = \frac{4\Omega_{\gamma 0}}{3\Omega_{b0}a} = \frac{4\Omega_{\gamma 0}}{3\Omega_{b0}} e^{-x}, \quad (3.41)$$

accounts for how photon pressure affects baryon motion. Since photons exert radiation pressure on baryons, this effect delays baryon decoupling relative to photon decoupling. The point when baryons stop being dragged by photons and begin to move under gravitational attraction alone is defined as $\tau_b = 1$, and the period between these two decoupling times is called the drag epoch. This is important for understanding baryon acoustic oscillations (BAO).

The visibility function $\tilde{g}(x)$ gives the probability density that a CMB photon last scattered at time x and is defined as:

$$\tilde{g}(x) = -\frac{d\tau}{dx} e^{-\tau(x)}. \quad (3.42)$$

This function peaks around photon decoupling, when $\tau(x) \approx 1$, meaning photons were transitioning from being frequently scattered to freely propagating. The width of $\tilde{g}(x)$ determines how sharply defined the time of photon decoupling is, hence why it is commonly called the surface of last scattering. It is also interesting to compute the first and second derivatives of the visibility function with respect to x , as \tilde{g}' provides insight into how rapidly recombination occurred, and \tilde{g}'' can tell us about how diffusion damping affects small-scale CMB anisotropies. **correct?**

mention baryon visibility function?

3.1.7. The sound horizon

The maximum comoving distance that a sound wave in the primordial plasma could have propagated from the beginning of the Universe is represented by the so-called sound horizon. It is defined as the integral of the sound speed over cosmic time:

$$s(x) = \int_0^x \frac{c_s(t')}{a(t')} dt' = \int_{-\infty}^x \frac{c_s(x')}{\mathcal{H}(x')} dx', \quad (3.43)$$

and is thus closely related to the particle horizon (eq. (2.21)). Here, c_s is the speed of sound in the tightly coupled photon-baryon plasma, hence the speed of a pressure wave propagating in the primordial fluid. It is given by

$$c_s(x) = \frac{c}{\sqrt{3(1 + R(x))}}, \quad (3.44)$$

where $R(x)$ is defined as in eq. (3.41). At early times, photons dominate, and $c_s \approx c/\sqrt{3}$, but as the Universe expands and baryons become more influential, c_s decreases.

A crucial quantity when studying the CMB is the sound horizon at decoupling, r_s , as this length scale is directly imprinted on the temperature power spectrum. More specifically, a commonly computed quantity in studies of the CMB is the angular acoustic scale, given in terms of r_s and the comoving distance to the last scattering surface $\chi_s = \eta_0 - \eta_s$ as

$$\theta_s = \frac{r_s}{\chi_s}. \quad (3.45)$$

Furthermore, the sound horizon at baryon decoupling, r_{drag} , is relevant for baryon acoustic oscillations in the large-scale distribution of galaxies. Accurately computing both sound horizons is therefore essential for making precise predictions about the observed large-scale structure of the Universe.

3.1.8. The baryon temperature

A common approximation in cosmology is to assume that the baryon temperature T_b follows the photon temperature $T_\gamma = T_{\text{CMB}}$ at all times due to rapid interactions between baryons and photons. However, Thomson scattering becomes too inefficient some time after decoupling, and the baryon temperature eventually starts evolving independently. Though this occurs relatively late in the recombination history, and thus has little effect on the CMB anisotropies, it is good to track the full evolution of T_b in order to ensure accuracy in the predictions.

The baryon temperature is also governed by the Boltzmann equation, and in a smooth, homogeneous universe, its evolution is given by:

$$\frac{dT_b}{dx} = 2 \left[\frac{\mu(x)}{m_e} \frac{d\tau_b}{dx} (T_b - T_{\text{CMB}}) - T_b \right], \quad (3.46)$$

Here, $\mu(x)$ is the mean molecular weight of baryons, including free electrons and all ions of Hydrogen and Helium, but it is a good approximation to simply set $\mu = m_{\text{H}}$ at all times x .

Eq. (3.46) is numerically unstable when $T_b \approx T_{\text{CMB}}$, so it's convenient to introduce

$$y = \frac{T_b}{T_{\text{CMB}}} - 1 \Rightarrow \frac{dy}{dx} = \frac{1}{T_{\text{CMB}}} \left[\frac{dT_b}{dx} - (y + 1) \frac{dT_{\text{CMB}}}{dx} \right], \quad (3.47)$$

and solve for this variable instead. Using that $T_{\text{CMB}} = T_{\text{CMB}0} e^{-x}$, and inserting eq. (3.46) into eq. (3.47), we thus get the following differential equation for y :

$$\frac{dy}{dx} = 1 + y \left[2 \frac{m_{\text{H}}}{m_e} \frac{d\tau_b}{dx} - 1 \right]. \quad (3.48)$$

3.2. Implementation details

3.2.1. The fiducial model

Adding to the cosmological parameters specified in section 2.2.1, I use the following parameters to compute the recombination and reionization history of the Universe:

$$\begin{aligned} Y_p &= 0.245, \\ z_{\text{reion}} &= 8.0, \\ \Delta z_{\text{reion}} &= 0.5, \\ z_{\text{He, reion}} &= 3.5, \\ \Delta z_{\text{He, reion}} &= 0.5. \end{aligned}$$

These are again based on best-fit values from the 2018 Planck results (see [Planck Collaboration et al. 2020](#)). They use a primordial Helium mass fraction of $Y_p = 0.2454$, the posterior mean predicted by Big Bang Nucleosynthesis, and state their estimate of the reionization redshift mid-point as $z_{\text{reion}} = 7.82 \pm 0.71$ based on 1σ limits on TT, TE, EE+lowE+lensing+BAO measurements. When modelling reionization, the rest of the parameters they use are the same as those stated here.

3.2.2. Main program structure

The free electron fraction, electron density, optical depths with derivatives, visibility functions with derivatives, sound horizon, and baryon temperature are all computed in the class `RecombinationHistory`, implemented in the source code and header files of the same name. This version differs more from Winther's original template than the `BackgroundCosmology`

class, but I have made sure to document it thoroughly without adding too much unnecessary text. **unprofessional sentence?** The same GSL-based ODE solver used previously is also used when solving for X_e (in the Peebles regime), τ , τ_b , \bar{g} , \bar{g}_b , s and T_b , and all of these solutions are interpolated using cubic splines. The results are written to file and visualized in `recombination.py`.

should I add a paragraph explaining the class methods?

3.2.3. Initial conditions

In the numerical implementation of the recombination history, careful selection of initial conditions is crucial for stable and accurate integration. The free electron fraction naturally starts at $X_e = 1$ in the early Universe when the medium is fully ionized. Furthermore, as we switch to the Peebles regime, the initial condition for X_e in eq. (3.25) is the last value computed in the Saha regime. From this, the free electron density n_e is determined using the baryon number density n_b , which is computed separately from cosmological parameters (eq. (3.9)).

For the optical depth, both the photon optical depth τ and the baryon optical depth τ_b are defined to be zero today. Since the optical depth is an integral that accumulates from past times until today, it is advantageous to integrate backward in time. This avoids truncation errors near $x = 0$ and ensures an accurate computation of the visibility function.

The sound horizon $s(x)$ requires an initial condition at early times. As mentioned in section 3.1.7, it is closely related to the conformal time η , which in the radiation-dominated era follows an analytical approximation (see section 2.2.3). Following an analogous reasoning, the initial condition for $s(x)$ thus becomes

$$s(x_{\text{start}}) = \frac{c_s(x_{\text{start}})}{H_0 \sqrt{\Omega_{r0}} e^{-2x_{\text{start}}}} \approx \frac{c_s(x_{\text{start}})}{\mathcal{H}(x_{\text{start}})}. \quad (3.49)$$

For the baryon temperature T_b , we initially set it equal to the photon temperature T_{CMB} . This is justified since Thomson scattering is highly efficient at maintaining thermal equilibrium between baryons and photons well into the Peebles regime. Since we solve for the variable $y = T_b/T_{\text{CMB}} - 1$, this means the initial condition for y is set to zero.

3.2.4. Integration limits and points

When integrating to solve for the different quantities, I used $x_{\text{min}} = -13.0$ and $x_{\text{max}} = 0.0$ as integration limits, since the evolutions beyond this region are of little physical significance.

correct to say? Also, using $x_{\text{max}} = 0.0$ as endpoint was most convenient, since the “initial condition” for the optical depth is $\tau(x=0) = 0$. Furthermore, I used 1 000 points when solving the system using only the Saha approximation, and 10 000 points when solving with both Saha and Peebles, to ensure a smoother transition between the two.

When splining the results I used $x_{\text{min}} = -12.0$ to avoid the more unstable starting point, and $x_{\text{max}} = 0.0$, since this endpoint is important to include in the analyzes. To ensure smooth visualization I used 12 001 points, corresponding to $\Delta x = 0.001$.

3.2.5. Tolerances

As mentioned in the previous section, I had to tune the number of integration points in order to avoid numerical instability in the transition between the Saha and Peebles regimes. Specifically,

the double derivative of the optical depth suffers from discontinuities if either too few or too many points are chosen. Also, I found that transitioning to the Peebles regime too late lead to the same effect, and ended up using $X_e < 0.9999$ as criterion.

Although I have decided to include Helium, the code also works with $Y_p = 0$. In that case, eq. (3.20) is used in the Saha regime when computing X_e , which has positive root

$$X_e = \frac{b}{2} \left(-1 + \sqrt{1 + \frac{4}{b}} \right), \quad b = \frac{1}{n_b} \left(\frac{m_e T_b}{2\pi} \right)^{3/2} e^{-\epsilon_0/T_b}. \quad (3.50)$$

In the early Universe T_b is very large, hence $b \ll 1$ since the exponential term dominates. Thus, $4/b \approx 0$, which leads to $X_e = 0$. Obviously, this is not the case at early times, and we may expand the square root around $4/b = 0$ to get $X_e \approx b/2(-1 + 1 + 2/b) = 1$. This is only viable in the very beginning of solving the system, and I have therefore set a tolerance of $4/b > 10^{-3}$ for when the above expression can be used to compute X_e .

As mentioned in section 3.1.3, one must solve iteratively for f_e in the Saha regime when using a non-zero Helium abundance. I chose to set $f_e = 1$ and $f_{e,\text{old}} = 0$ to begin with, then use $|f_e - f_{e,\text{old}}| < 10^{-10}$ as stopping criterion to ensure that it had properly converged. This is not numerically challenging, so the low tolerance has negligible effect on the computation speed.

word different?

When solving for the baryon temperature T_b , we have a set of coupled differential equations for X_e and y in the Peebles regime becomes. The ODE for y is very stiff in the beginning, and since we expect the baryon and photon temperatures to be identical until well after recombination, I have chosen to simply set $T_b = T_{\text{CMB}}$ in the differential equation for X_e until some threshold value of x . This can be passed as an argument to the right-hand side method for the Peebles ODE, with default value `x_tol=-7.0` (which is what I have used to produce my results). Furthermore, to aid in the stability of the differential equations I have made it so that the absolute and relative tolerances of the ODE solver are changed from $\epsilon_{\text{abs}} = \epsilon_{\text{rel}} = 10^{-7}$ to $\epsilon_{\text{abs}} = \epsilon_{\text{rel}} = 10^{-12}$ in case we solve for T_b .

3.2.6. Testing numerical stability

A good way to check that the computed quantities are reasonable is to compute the integrals of \tilde{g} and \tilde{g}_b from x_{min} to x_{max} , since these are probability density functions and must therefore integrate up to unity. By summing the splined values and dividing by the number of points used for integrating, I found that

$$\int_{x_{\text{min}}}^{x_{\text{max}}} \tilde{g}(x) dx = 1.0 + 9.6 \times 10^{-8},$$

$$\int_{x_{\text{min}}}^{x_{\text{max}}} \tilde{g}_b(x) dx = 1.0 + 6.7 \times 10^{-9},$$

which of course corresponds to relative errors of $9.6 \times 10^{-6} \%$ and $6.7 \times 10^{-7} \%$, respectively. redundant? This greatly validates most of the numerical solutions, as the visibility functions depend on the optical depths, which in turn depend on the free electron fraction.

3.3. Results and discussions

3.3.1. Electron fraction and number density

In figure 3.1, I have plotted the free electron fraction, X_e (left subplot), and the electron number density, n_e (right subplot), as

functions of x . Initially, we observe that $X_e \lesssim 1.2$, reflecting a fully ionized Universe where both Hydrogen and Helium are ionized. The free electron fraction slightly exceeds 1 due to the contribution of Helium. As the Universe expands and cools, recombination progresses in stages. Around $x \approx -9$, doubly ionized Helium (He^{++}) captures an electron and transitions to singly ionized Helium (He^+). Shortly afterward, at $x \approx -8$, He^+ recombines into neutral Helium (He). Hydrogen recombination occurs later, around $x \approx -7$, where X_e undergoes a steep decline as most free electrons combine with protons to form neutral Hydrogen. This marks Hydrogen recombination as the dominant process in determining the final ionization state of the Universe.

The impact of these recombination events is also evident in the evolution of the electron number density. During Helium recombination, n_e follows the expected trend of volume dilution with no significant deviations, indicating that Helium recombination has a minimal effect on the overall number density. However, during Hydrogen recombination, n_e drops by approximately four orders of magnitude, demonstrating the rapid capture of electrons by protons. A similar trend can be seen at later times: although He^+ reionization leads to an increase in the free electron fraction, its effect on the total number density is negligible compared to the large increase that occurs during the first reionization period.

By turning off reionization, I determined the freeze-out abundance of free electrons to be:

$$X_e \approx 2.7 \times 10^{-4},$$

$$n_e \approx 5.2 \times 10^{-5} \text{ m}^{-3}.$$

These values align well with standard recombination theory, which predicts a residual ionized fraction X_e on the order of 10^{-3} to 10^{-4} . Although this small asymptotic value is difficult to observe directly in today's highly reionized Universe, it plays an important role in our understanding of the thermal history between recombination and reionization. The existence of this residual electron population reflects the fact that photons with energies exceeding the ionization threshold remain present after recombination. These high-energy photons can continue to ionize a small fraction of Hydrogen atoms, thereby preventing complete neutralization.

3.3.2. Optical depths

Figure 3.2 illustrates the evolution of the optical depth $\tau(x)$ (blue), its first derivative $-\tau'(x)$ (red), and its second derivative $\tau''(x)$ (green) as functions of x . These quantities are shown for both photons (darker colors) and baryons (lighter colors). We see that the photon optical depth τ is initially large, reflecting the fact that photons are tightly coupled to the baryon-electron plasma due to frequent Thomson scattering. Around decoupling we see a rapid drop in τ , since the photons stop noticing the baryons. This is also visible from the steep negative peak in $-\tau'$, which marks the rapid decline in the scattering probability.

The second derivative τ'' provides further insight into the recombination process. We see two smaller peaks right before the dominant Hydrogen recombination, corresponding to the transitions of $\text{He}^{++} \rightarrow \text{He}^+$ and $\text{He}^+ \rightarrow \text{He}$, which highlights the changes in the free electron fraction seen in figure 3.1. Though subtle, these peaks indicate sudden drops in $-\tau'$, demonstrating that X_e does not decrease monotonically but rather in distinct stages due to the sequential recombination of Helium and Hydrogen.

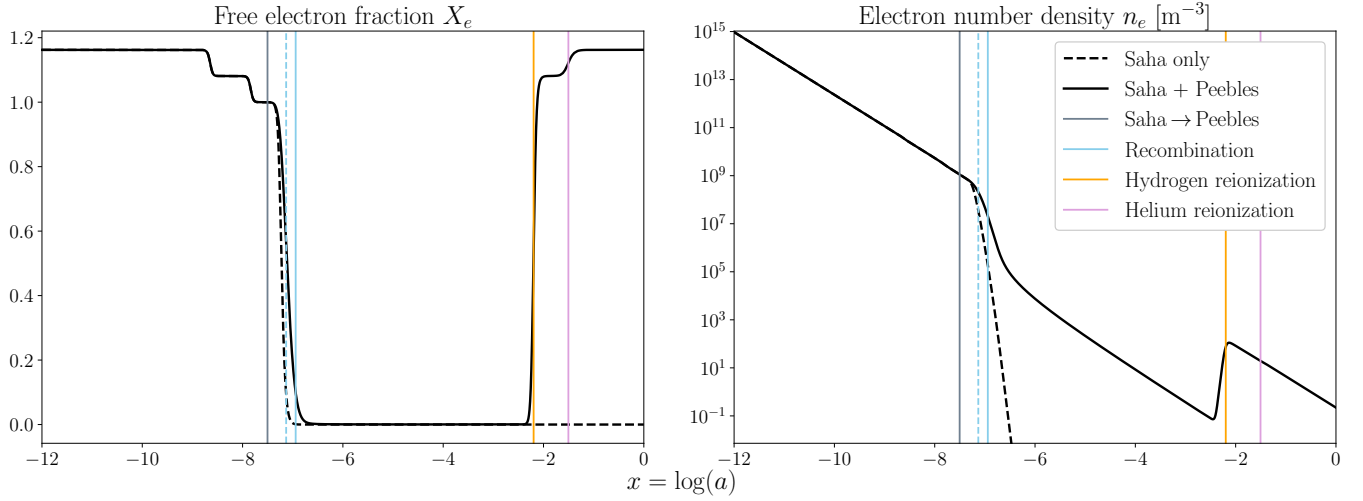


Fig. 3.1. The evolution of the free electron fraction X_e (left) and the free electron number density n_e (right) as functions of $x = \log(a)$. The dashed blue line marks the time of recombination estimated using only the Saha approximation, while the solid line shows the result from solving the Peebles equation. The significant difference illustrates the limitations of assuming equilibrium.

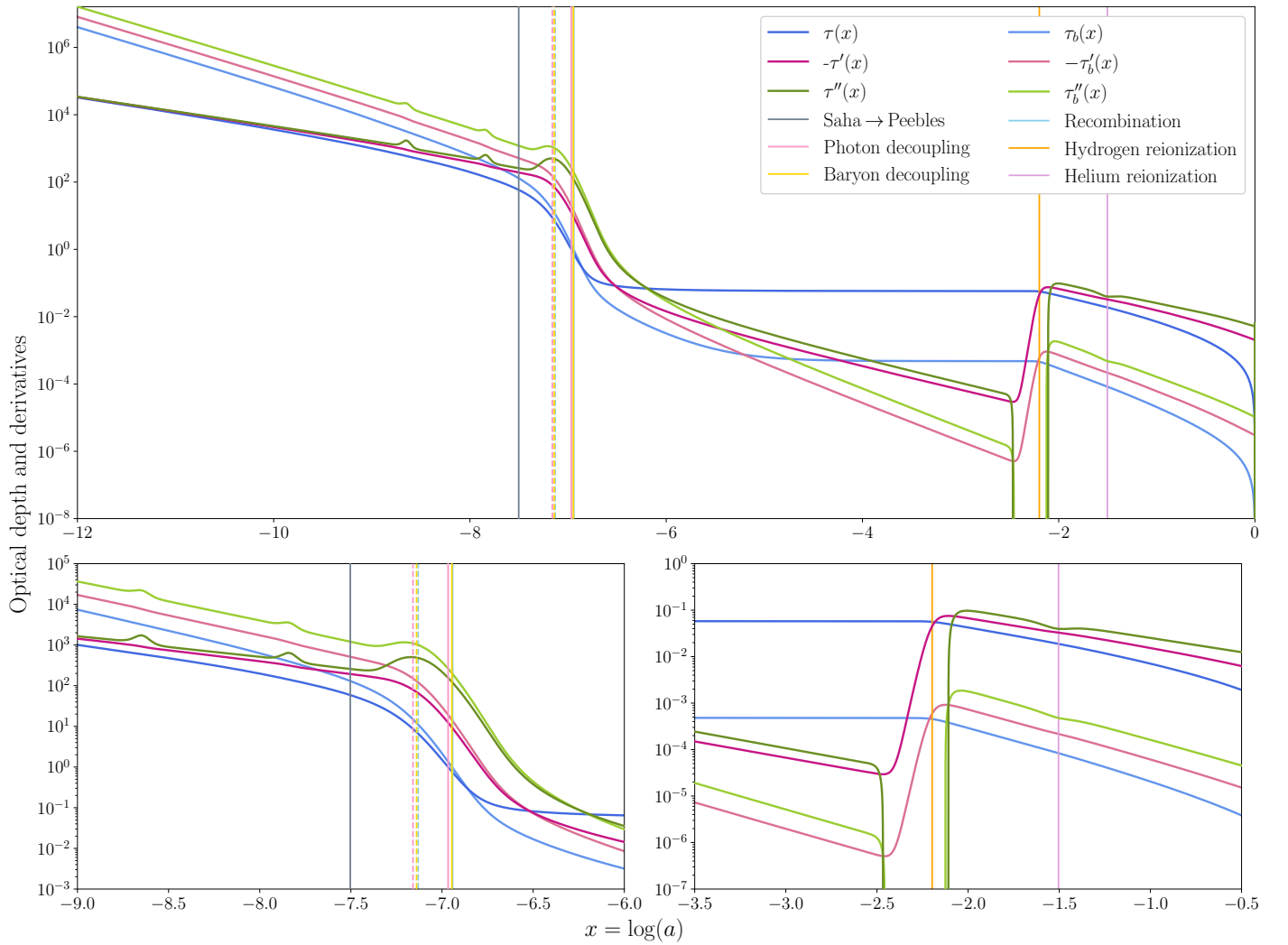


Fig. 3.2. The evolution of the optical depth τ (blue), its first derivative $-\tau'$ (red), and its second derivative τ'' (green) for both photons (darker lines) and baryons (lighter lines). The bottom left subplot shows the evolutions of these quantities around decoupling and recombination, while the bottom right subplot highlights their changes during the epoch of reionization. The sharp drop in τ marks photon decoupling, after which photons free-stream. In contrast, the gradual decline in τ_b indicates the prolonged influence of radiation pressure on baryons during the drag epoch.

After recombination, τ levels off and remains nearly constant, meaning that photons are no longer frequently scattering. This corresponds to the transition to CMB free-streaming, where the photons released at decoupling travel largely undisturbed throughout the Universe. However, at $x \lesssim -2$ we observe a sudden increase in $-\tau'$, accompanied by a sharp drop in τ'' , corresponding to Hydrogen reionization. This phase is driven by ionizing radiation from early stars, which rapidly increases the free electron fraction, as reflected in the jumps in X_e and n_e in figure 3.1. The optical depth τ then enters a plateau. A second, smaller bump at $x \approx -1.5$ arises from Helium reionization, caused by high-energy photons from quasars that fully ionize singly ionized Helium (see e.g. ? for updated analyzes in light of recent JWST data).

To understand the reionization plateau, consider a photon emitted at redshift $z < z_{\text{reion}}$. Since most Hydrogen is ionized, it has a non-negligible probability of Thomson scattering on its way to us. This probability accumulates over time, making the optical depth larger for photons emitted further in the past. However, for photons emitted in the neutral era between recombination and reionization ($z_{\text{rec}} \gg z > z_{\text{reion}}$), the scattering probability remains constant, leading to a roughly constant optical depth in this regime. The optical depth at reionization is often a more relevant quantity than the precise redshift of reionization. From my computed spline, I found this value to be $\tau_{\text{reion}} = 0.0561$, which perfectly matches the Planck 2018 result: based on TT,TE,EE+lowE+lensing+BAO measurements, [Planck Collaboration et al. \(2020\)](#) found $\tau_{\text{reion}} = 0.0561 \pm 0.0071$.

The baryon optical depth τ_b follows a similar evolution to the photon optical depth but starts from a significantly higher value. This reflects the large photon-to-baryon ratio, implying that baryons have an even shorter mean free path than photons in the tightly coupled plasma. Around decoupling, τ_b also undergoes a decline but does so more gradually due to the extended drag epoch, during which residual interactions between baryons and photons delay the onset of independent baryon motion. As seen in the photon case, Hydrogen and Helium reionization lead to a delayed but noticeable increase in τ'_b , though the effect is less pronounced. Since baryons are non-relativistic, they are less affected by changes in the free electron fraction compared to photons, resulting in a weaker response to reionization.

3.3.3. Visibility functions

In figure 3.3, I have plotted the photon (black) and baryon (grey) visibility functions $\tilde{g}(x)$ and $\tilde{g}_b(x)$ (top), their first derivatives $\tilde{g}'(x)$ and $\tilde{g}'_b(x)$ (middle), and their second derivatives $\tilde{g}''(x)$ and $\tilde{g}''_b(x)$ (bottom) as functions of x . The interval $x \in [-12, -8]$ has been omitted, as all these quantities remain identically zero in this range. The sharp peaks of the visibility functions around $x \approx -7$ coincide with the estimated decoupling times, confirming that the last scattering event occurred within this window. As expected, \tilde{g}_b peaks slightly later than \tilde{g} , which aligns with the fact that the baryon-photon drag epoch extends beyond photon decoupling. Furthermore, the peak of \tilde{g}_b is significantly larger than that of \tilde{g} , reflecting the fact that $\tau_b > \tau$ and $-\tau'_b > -\tau'$ in this region, as seen in figure 3.2. This behavior is a direct consequence of the stronger coupling between baryons and photons prior to baryon decoupling.

As discussed in section 3.1.6, the width of the main peak in the photon visibility function $\tilde{g}(x)$ determines the thickness of the last scattering surface: a narrower peak would indicate an abrupt transition to free-streaming, while a broader peak suggests a more extended decoupling period. The zero-crossing of

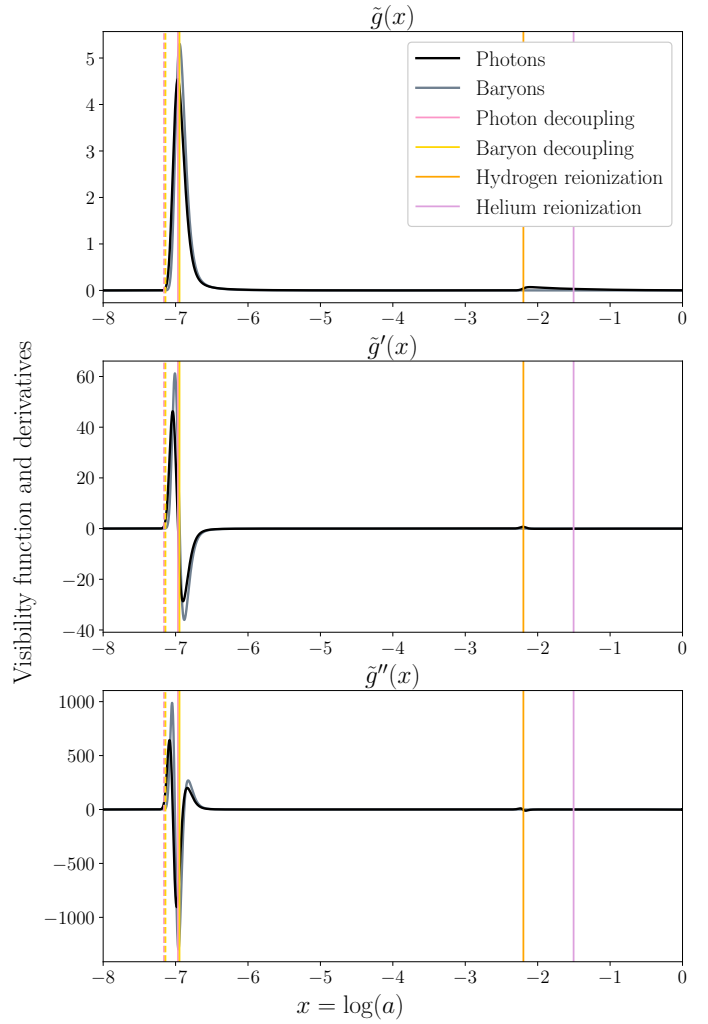


Fig. 3.3. The visibility function $\tilde{g}(x)$ (top), its first derivative $\tilde{g}'(x)$ (middle), and its second derivative $\tilde{g}''(x)$ (bottom), plotted for both photons (black) and baryons (grey). The sharp peak in \tilde{g} defines the last scattering surface, while the first derivative's zero-crossing confirms the rapid transition.

$\tilde{g}'(x)$ corresponds to the moment of the steepest decline in the visibility function, marking the rapid transition in photon scattering probability. This aligns with the moment of photon decoupling, confirming that the transition was well-defined but not instantaneous. The strong negative dip in the second derivative $\tilde{g}''(x)$ around $x \approx -7$ quantifies the sharpness of this transition, reinforcing that photon decoupling occurred within a narrow but finite time interval.

At later times, around $x \lesssim -2$, Hydrogen reionization causes a secondary, broad increase in $\tilde{g}(x)$, reflecting the renewed interaction between photons and free electrons. However, this increase is significantly smaller than at recombination, indicating that only a fraction of CMB photons were re-scattered during this epoch. The visibility function barely changes during the subsequent reionization of singly ionized Helium to doubly ionized Helium, as expected from the negligible impact of this process on the optical depths and their first derivatives. Unlike at decoupling, where the changes in \tilde{g}_b and its derivatives were more pronounced than those in \tilde{g} , the effects at reionization are significantly weaker. This is a direct result of the much smaller values of τ_b and τ'_b in this region, implying that baryons experienced minimal drag from photon interactions during reionization.

maybe have zoomed in plot in appendix?

3.3.4. Important time stamps and horizons

Table 3.1 presents the computed values of x , redshift z , cosmic time t , conformal time (particle horizon) η , and sound horizon s corresponding to photon and baryon decoupling, the changes that occurred during the drag epoch in between the two, as well as recombination. The values are given both for calculations using only the Saha approximation and for the more accurate approach that includes the full Peebles equation. As expected, photon decoupling (where τ falls to unity) and recombination (when X_e drops below 0.1) occur at nearly identical times. This is because photons cease scattering once neutral Hydrogen forms, making the two processes tightly linked. However, recombination happens slightly later because a residual fraction of free electrons persists even after photons transition to free-streaming. Baryon decoupling occurs between the two, as evident from figures 3.2 and 3.3.

The Saha approximation alone predicts earlier times of recombination and decoupling, consistent with the steeper drop in the free electron fraction observed in figure 3.1. This discrepancy arises because the Saha equation assumes instantaneous thermal equilibrium, meaning ionization and recombination are treated as occurring instantaneously when crossing equilibrium thresholds. However, in reality, recombination is a non-equilibrium process, as captured by the Peebles equation, which accounts for the slower capture of electrons by protons in an expanding universe.

The difference in sound horizons between the two approaches highlights the impact of an earlier recombination. Since sound waves in the tightly coupled photon-baryon plasma define the characteristic scale of acoustic oscillations, an earlier recombination results in a slightly smaller sound horizon. This has direct consequences for the CMB anisotropy spectrum, as the first acoustic peak corresponds to the largest mode that fits within the sound horizon at decoupling. A smaller sound horizon shifts the peak positions and alters the angular scale of the acoustic features in both the CMB power spectrum and the BAO in the matter power spectrum. This clearly demonstrates the necessity of using the Peebles equation to accurately model recombination, as relying on the Saha approximation alone leads to artificially early decoupling and incorrect predictions for the CMB and BAO scales.

Figure 3.4 illustrates the evolution of the sound horizon $s(x)$, with the estimated time of recombination marked to highlight where its growth gets stunted. In the early Universe, the sound horizon increases rapidly due to the high sound speed in the tightly coupled photon-baryon fluid. This is a direct consequence of the nearly relativistic equation of state of the plasma, where the sound speed c_s remains close to $c/\sqrt{3}$. However, around recombination, the pressure support from photons is significantly reduced, allowing matter to cluster more freely and leading to a decrease in the sound speed. Consequently, the growth of the sound horizon flattens out as baryons decouple from photons and begin falling into dark matter potential wells, setting the scale of BAO in the later Universe.

In Planck Collaboration et al. (2020) they estimate the redshifts at photon and baryon decoupling as $z_s = 1089.92 \pm 0.25$ and $z_{\text{drag}} = 1059.94 \pm 0.30$, respectively, based on 1σ limits from TT,TE,EE+lowE+lensing measurements. The corresponding sound horizons are estimated to be $r_s = 144.43 \pm 0.26$ Mpc and $r_{\text{drag}} = 149.09 \pm 0.26$ Mpc. My inferred redshifts are sys-

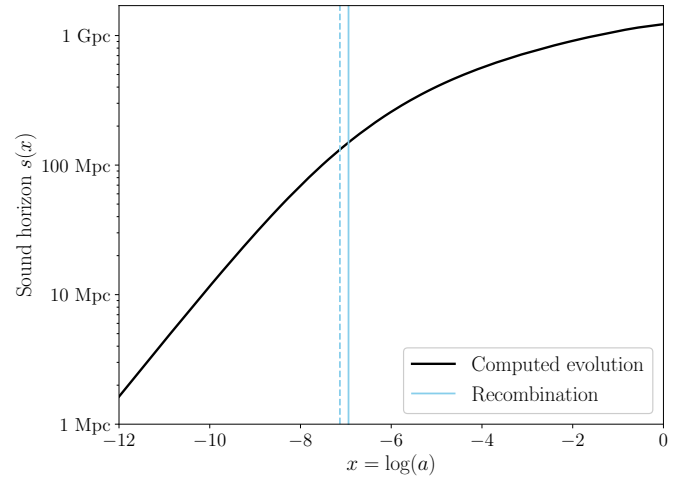


Fig. 3.4. The evolution of the sound horizon $s(x)$ as a function of $x = \log(a)$. The rapid early growth reflects the high sound speed in the tightly coupled photon-baryon plasma, while the flattening at recombination marks the transition to the so-called dark ages. correct?

tematically lower, though the computed sound horizons are in reasonable agreement. The estimate for r_{drag} is particularly close to the Planck value, but the discrepancy in redshift suggests differences in numerical methods and cosmological model assumptions. A possible source of discrepancy could be the specific recombination model used; Planck employs Recfast add citation?, which incorporates additional refinements beyond the Peebles equation, such as corrections for two-photon decays and non-equilibrium effects. Differences in how reionization is handled (e.g., the choice of $z_{\text{reion}} = 8$ in my calculations vs. Planck's $z_{\text{reion}} = 7.64$) could also slightly shift inferred parameters.

correct? or irrelevant?

Using the value for the particle horizon at photon decoupling presented in table 3.1 (Saha + Peebles approach) and the present-day particle horizon from table 2.1 (numerical value), the comoving distance to the last scattering surface is found to be $\chi_s \approx 13904.51$ Mpc. With my computed sound horizon at decoupling of $r_s \approx 146.66$ Mpc, this gives an angular acoustic scale of $100\theta_s \approx 1.0548$. This is slightly larger than the Planck result of $100\theta_s = 1.0411 \pm 0.0003$, falling outside their reported uncertainty. However, it should be noted that my inferred value lacks the precision implied by this number of significant digits due to numerical approximations. Potential sources of uncertainty include the finite resolution of the numerical integration, the choice of interpolation method for the visibility function, and approximations made in the recombination model.

3.3.5. Baryon temperature evolution

Figure 3.5 illustrates the evolution of the baryon temperature $T_b(x)$ (black line) compared to the photon (CMB) temperature $T_{\text{CMB}}(x)$ (grey line). Before recombination the baryon temperature closely follows the photon temperature due to strong Thomson scattering between electrons and CMB photons, which ensures thermal equilibrium. In this regime, both temperatures scale as $T \propto a^{-1}$, as expected for a relativistic plasma. However, baryons begin to cool independently some time after recombination, around $x \approx -6$. At this point, the baryon temperature transition from the radiation-like scaling to an adiabatic evolu-

Table 3.1. Table of key cosmological time stamps, showing photon and baryon decoupling, the changes that occur inbetween (the drag epoch), and recombination, along with their corresponding redshifts, cosmic times, conformal times (particle horizons), and sound horizons. The Saha-only results differ significantly from the full solution, underestimating recombination time due to its equilibrium assumption.

| Quantity | Method | Photon decoupling | Baryon decoupling | Drag epoch | Recombination |
|--------------|----------------|-------------------|-------------------|------------|---------------|
| x | Saha only | -7.16 | -7.14 | 0.02 | -7.13 |
| | Saha + Peebles | -6.97 | -6.95 | 0.02 | -6.94 |
| z | Saha only | 1291.70 | 1260.11 | -31.59 | 1249.29 |
| | Saha + Peebles | 1064.44 | 1037.76 | -26.68 | 1033.21 |
| t [kyr] | Saha only | 279.19 | 291.19 | 11.99 | 295.48 |
| | Saha + Peebles | 387.17 | 404.02 | 16.85 | 407.01 |
| η [Mpc] | Saha only | 246.80 | 251.49 | 4.69 | 253.14 |
| | Saha + Peebles | 285.49 | 290.92 | 5.43 | 291.87 |
| s [Mpc] | Saha only | 128.90 | 131.09 | 2.19 | 131.85 |
| | Saha + Peebles | 146.66 | 149.10 | 2.44 | 149.53 |

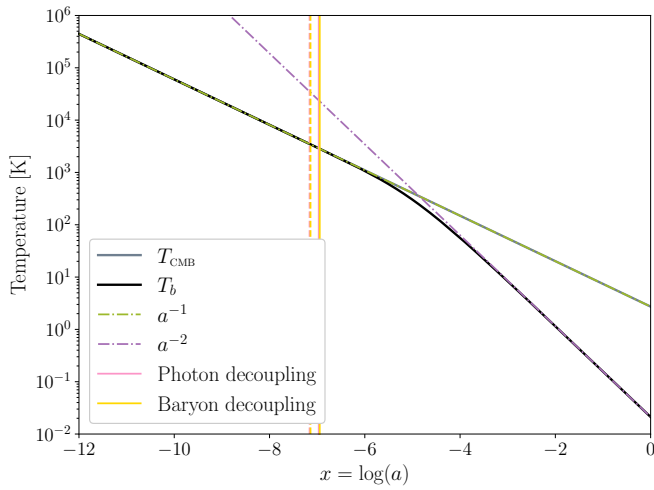


Fig. 3.5. The evolution of the baryon temperature $T_b(x)$ (black) compared to the photon temperature $T_{\text{CMB}}(x)$ (grey). The two temperatures track each other closely before recombination due to strong Thomson scattering. Some time after decoupling, baryons start to cool adiabatically as $T_b \propto a^{-2}$ (purple dashed line), while photons continue to cool as $T_{\text{CMB}} \propto a^{-1}$ (green dashed line).

tion, where $T_b \propto a^{-2}$, since the baryons no longer receive energy from photons and instead evolve as a non-relativistic gas in an expanding universe. This is directly linked to the drop in optical depth observed in figure 3.2. The delay between decoupling and the point where the two diverge explains why τ_b declines more gradually than τ , extending the impact of photon pressure beyond the formal decoupling time.

I found the baryon temperature to be $T_{b0} \approx 21$ mK, which is only about $\sim 7 - 8\%$ of the measured CMB temperature today. This result is consistent with theoretical expectations, given the a^{-2} scaling of T_b after $x \approx 6$ compared to the a^{-1} scaling of T_{CMB} . However, unlike the CMB temperature, which follows a nearly perfect blackbody distribution with only small-scale anisotropies encoding information about early-universe physics, the baryon temperature is not a meaningful global quantity today. This is because matter has strongly clustered since decoupling, leading to highly non-linear structure formation. Most of the baryonic content is no longer in a diffuse, cold state, but con-

centrated into dense regions such as stars, galaxies, and the hot intergalactic medium. There are very few regions of truly diffuse baryonic gas with temperatures as low as the mean value presented here, though such cold gas remains an active area of research in extragalactic astronomy (see e.g., Tumlinson et al. (2017) and Nelson et al. (2020) about the cold circumgalactic medium).

The temperature deviation between photons and baryons introduces a minor correction to the photon-baryon sound speed, which in principle affects the evolution of acoustic oscillations. However, since recombination is complete before T_b and T_{CMB} significantly diverge, this effect is minimal. For precision calculations of the CMB power spectrum, including the evolution of T_b can slightly refine the modeling of BAO, but its impact on large-scale anisotropies will likely remain small, as mentioned in section 3.1.8.

4. Milestone III: Perturbations

Having established the background evolution of the universe and the recombination history in the previous milestones, I now turn to the evolution of cosmological perturbations, which describe how small fluctuations in density and temperature grew from the early Universe into the large-scale structures we observe today. This step is essential for understanding the formation of CMB anisotropies, as well as the distribution of galaxies and clusters in the late Universe.

In this milestone, I numerically solve the Einstein-Boltzmann equations to track the evolution of perturbations in different components of the Universe, including photons, neutrinos, baryons, and cold dark matter. By evolving these perturbations across different Fourier modes, I construct time-dependent solutions for key physical quantities such as density and velocity perturbations, temperature fluctuations, and gravitational potentials. Additionally, I account for the tight-coupling approximation at early times to handle numerical instabilities and ensure accurate solutions. The results from this milestone provide the foundation for computing the CMB power spectrum in the next step, allowing us to directly compare theoretical predictions with observations.

mention that we use linear perturbation theory?

4.1. Theoretical framework

4.1.1. Perturbations in the Newtonian gauge

maybe rename section

The perturbed Einstein equations for scalars, vectors, and tensors decouple at linear order, allowing us to study them separately. In this work, I primarily focus on scalar perturbations, which correspond to density fluctuations and are responsible for structure formation. Vector perturbations (vorticity) are not generated by inflation and decay rapidly due to cosmic expansion, hence they are irrelevant when computing the CMB. Furthermore, tensor perturbations (gravitational waves) are a key prediction of inflation and is therefore a topic I revisit in the next milestone.

To simplify the perturbation equations, I work in the Newtonian gauge, where the metric is diagonal:

$$ds^2 = -(1 + 2\Psi)dt^2 + a^2(1 + 2\Phi)\delta_{ij}dx^i dx^j. \quad (4.1)$$

Here, Ψ and Φ are the gravitational potentials, which describe scalar perturbations to the metric and play analogous roles to the Newtonian potential in classical gravity. This is another perk of working in the Newtonian gauge, as it allows for more intuitive physical interpretation while keeping the full relativistic structure of general relativity. correct to say this? More specifically, Ψ represents the perturbation to the time-time component of the metric and acts as the gravitational potential experienced by non-relativistic particles, while Φ appears in the spatial metric perturbations and affects the expansion of space.

The perturbation equations take the form of coupled partial differential equations in real space, which are not trivial to solve. To simplify the problem, we transform them into Fourier space, where they become a system of ordinary differential equations for each wave mode. In Fourier space, spatial derivatives transform as:

$$\nabla u(x) \rightarrow ik\tilde{u}(k), \quad (4.2)$$

where \mathbf{k} is the comoving wave vector of the perturbation. This Fourier decomposition allows us to track the evolution of perturbations across different scales and study their behavior from superhorizon to subhorizon regimes.

4.1.2. Photons

The evolution of CMB anisotropies is governed by perturbations in the photon distribution function. Since photons are massless, they follow null geodesics in a perturbed metric. For a photon with four-momentum P^μ and energy $E = p$, expanding the Christoffel symbols in the geodesic equation leads to:

$$\frac{dP^0}{d\lambda} + \Gamma_{\mu\nu}^0 P^\mu P^\nu = 0 \quad (4.3)$$

$$\Rightarrow \frac{dp}{dt} = \frac{1}{P_0} \frac{dp}{d\lambda} \simeq -p \left[H + \frac{\partial\Phi}{\partial t} + \frac{\partial\Psi}{\partial x^i} \frac{\hat{p}^i}{a} \right]. \quad (4.4)$$

show this? This equation describes how the photon energy changes due to both cosmic expansion (the Hubble term H) and metric perturbations. Integrating from recombination to today gives the perturbation to the photon energy in terms of its initial value:

$$\left(\frac{\delta p}{p} \right)_0 = \left(\frac{\delta p}{p} \right)_{\text{rec}} + (\Psi_{\text{rec}} - \Psi_0) + \int_{t_{\text{rec}}}^{t_0} \left[\frac{\partial\Psi}{\partial t} - \frac{\partial\Phi}{\partial t} \right] dt. \quad (4.5)$$

Eq. (4.5) encodes two key effects that shape CMB anisotropies. The first of these is the Sachs-Wolfe effect: the gravitational redshift of photons due to metric perturbations at the last scattering surface, corresponding to the term $(\Psi_{\text{rec}} - \Psi_0)$. More specifically, this represents the change in the gravitational potential from recombination to today. Furthermore, the last term represents the time variation of the metric perturbations $(\partial_t\Psi - \partial_t\Phi)$, which affects photons' energies as they travel through evolving potential wells. This is called the integrated Sachs-Wolfe (ISW) effect, and is most important in the late Universe when dark energy becomes significant.

To describe perturbations in the CMB systematically, we introduce the photon temperature perturbation, defined as:

$$T = \bar{T}(1 + \Theta), \quad (4.6)$$

where $\Theta = \delta T / \bar{T}$ represents small deviations from the mean photon temperature. present different? This perturbation generally depends on time, space, the magnitude, and direction of the photon momentum. However, since Thomson scattering only affects the direction of the photon momentum to first order, we can express the perturbation as $\Theta(t, \mathbf{x}, \hat{p})$, eliminating explicit dependence on p . Furthermore, expanding the distribution function for photons in the limit $\Theta \ll 1$ gives:

$$f = \frac{1}{e^{p/\bar{T}(1-\Theta)} - 1} \simeq \bar{f} + \Theta p \frac{\partial \bar{f}}{\partial p}, \quad (4.7)$$

where

$$\bar{f} = \frac{1}{e^{p/\bar{T}} - 1}. \quad (4.8)$$

Since the chemical potential $\mu = 0$ for photons, this follows directly from the Bose-Einstein distribution (eq. (3.1)). Subtracting the background evolution from the full Boltzmann equation (3.3) leads to the first-order perturbed Boltzmann equation for photons:

$$\frac{df}{d\lambda} = -p^2 \frac{\partial \bar{f}}{\partial p} \left[\frac{\partial\Theta}{\partial t} + \frac{\partial\Theta}{\partial x^i} \frac{\hat{p}^i}{a} + \left(\frac{\partial\Phi}{\partial t} + \frac{\partial\Psi}{\partial x^i} \frac{\hat{p}^i}{a} \right) \right] = C[f]. \quad (4.9)$$

show this more explicitly?

As discussed extensively in the previous milestone, the dominant interaction term for photons is Thomson scattering with free electrons. too repetitive? If we ignore polarization and the angular dependence of the cross section, the collision to first order in perturbation theory simplifies to

$$C[f] = -p^2 \frac{\partial \bar{f}}{\partial p} n_e \sigma_T (\Theta_0 - \Theta + \hat{p} \cdot \mathbf{v}_b). \quad (4.10)$$

Here, \mathbf{v}_b is the baryon velocity, which describes how fast electrons (and protons) are moving, and

$$\Theta_0 = \frac{1}{4\pi} \int \Theta d\Omega_{\hat{p}} = \frac{1}{2} \int_{-1}^1 \Theta d\mu, \quad (4.11)$$

is the monopole moment of the photon distribution, which describes the local temperature averaged over all directions. The integration variable μ is simply the cosine of the angle between the wavevector \mathbf{k} and the photon direction:

$$\mu = \hat{p} \cdot \frac{\mathbf{k}}{k}. \quad (4.12)$$

Thus, inserting this into eq (4.9) we arrive at the perturbed Boltzmann equation for photons:

$$\frac{\partial \Theta}{\partial t} + \frac{\partial \Theta}{\partial x^i} \frac{\hat{p}^i}{a} + \left(\frac{\partial \Phi}{\partial t} + \frac{\partial \Psi}{\partial x^i} \frac{\hat{p}^i}{a} \right) = n_e \sigma_T (\Theta_0 - \Theta + \hat{p} \cdot \mathbf{v}_b). \quad (4.13)$$

This equation tells us that when Thomson scattering is efficient, photons from different directions have the same temperature, enforcing $\Theta \approx \Theta_0$ locally.

Since CMB perturbations are naturally described in Fourier space [correct to say this?](#), it is convenient to make use of \mathbf{k} and μ . The baryon velocity is curl-free, so in Fourier space it simplifies to

$$\mathbf{v}_b = i v_b \frac{\mathbf{k}}{k}. \quad (4.14)$$

With this, the Boltzmann equation transforms into

$$\frac{\partial \Theta}{\partial t} + \frac{i k \mu}{a} \Theta + \left(\frac{\partial \Phi}{\partial t} + \frac{i k \mu}{a} \Psi \right) = n_e \sigma_T \left(\Theta_0 - \Theta + i \mu v_b - \frac{3 \mu^2 - 1}{4} \Pi \right), \quad (4.15)$$

where the additional term

$$\Pi = \Theta_2 = -\frac{1}{2} \int_{-1}^1 \Theta \frac{3 \mu^2 - 1}{2} d\mu, \quad (4.16)$$

accounts for the angular dependence of Thomson scattering.

4.1.3. Multipole expansions

As mentioned in the previous section, the equation governing the evolution of the photon temperature perturbation depends explicitly on the angular direction of the photon momentum. To obtain a more manageable system of equations, it is convenient to expand the angular dependence of the perturbation $\Theta(t, \mathbf{k}, \mu)$ in terms of Legendre polynomials, leading to a hierarchy of equations known as the Boltzmann hierarchy. This expansion is particularly useful since the CMB anisotropies are naturally expressed in terms of spherical harmonics, which are closely related to Legendre polynomials. Thus, we write:

$$\Theta(t, \mathbf{k}, \mu) = \sum_{\ell=0}^{\infty} \frac{2\ell+1}{i^\ell} \Theta_\ell(t, \mathbf{k}) P_\ell(\mu), \quad (4.17)$$

where $P_\ell(\mu)$ are the Legendre polynomials, and Θ_ℓ are the multipole moments of the photon distribution function, defined as:

$$\Theta_\ell(t, \mathbf{k}) = \frac{i^\ell}{2} \int_{-1}^1 \Theta(t, \mathbf{k}, \mu) P_\ell(\mu) d\mu. \quad (4.18)$$

The first few moments in the multipole expansion have clear physical interpretations. As we have already seen in eq. (4.10), the $\ell = 0$ term corresponds to the monopole moment, which is directly related to the density contrast of radiation via $\delta_\gamma = 4\Theta_0$. Furthermore, the $\ell = 1$ term describes the dipole moment, which tells us about the velocity of the photon perturbations through $v_\gamma = -3\Theta_1$. [word different?](#) Lastly, $\ell = 2$ corresponds to the quadrupole moment of the photon distribution and is closely associated with the anisotropic stress, which we will get back to. Higher-order multipoles describe increasingly finer angular variations in the photon distribution, though they are less intuitive to interpret physically.

To derive the evolution equations for the multipoles, we take moments of the Boltzmann equation for photons. This requires the orthogonality relation for Legendre polynomials,

$$\mu P_\ell = \frac{\ell+1}{2\ell+1} P_{\ell+1} + \frac{\ell}{2\ell+1} P_{\ell-1}. \quad (4.19)$$

Multiplying eq. (4.15) by $(i^\ell/2)P_\ell$ and integrating over μ allows us to obtain a coupled hierarchy of equations. For $\ell = 0, 1, 2, \dots$, this results in:

$$\Theta'_0 = -\frac{ck}{\mathcal{H}} \Theta_1 - \Phi', \quad (4.20)$$

$$\Theta'_1 = \frac{ck}{3\mathcal{H}} \Theta_0 - \frac{2ck}{3\mathcal{H}} \Theta_2 + \frac{ck}{3\mathcal{H}} \Psi + \tau' \left[\Theta_1 + \frac{1}{3} v_b \right], \quad (4.21)$$

$$\Theta'_\ell = \frac{ck}{(2\ell+1)\mathcal{H}} \left[\ell \Theta_{\ell-1} - (\ell+1) \Theta_{\ell+1} \right] + \tau' \left[\Theta_\ell - \frac{1}{10} \Pi \delta_{\ell,2} \right], \quad \ell \geq 2. \quad (4.22)$$

Here, derivatives are taken with respect to x , and the optical depth derivative τ' appears as it was defined in eq. (3.39).

Eq. (4.20) corresponds to the perturbed continuity equation for photons, which ensures conservation of particle number. Furthermore, eq. (4.21) describes the evolution of the photon dipole and is equivalent to the Euler equation, accounting for the anisotropic stress through the quadrupole term, as well as the momentum transfer between photons and baryons via the last term. This ensures that the baryon velocity remains equal to the photon velocity in the tight-coupling regime, which I come back to in section 4.1.10. [word different?](#)

Since the Boltzmann hierarchy contains an infinite number of coupled equations, solving the full system numerically is impossible. Fortunately, at sufficiently high multipoles, the moments decrease in amplitude, allowing for an approximation. However, a naive truncation, such as setting all moments beyond some ℓ_{\max} to zero, would introduce errors that propagate to lower multipoles. Instead, the hierarchy is truncated by modifying the equation for the highest included multipole:

$$\Theta'_{\ell_{\max}} = \frac{ck}{\mathcal{H}} \Theta_{\ell_{\max}-1} - c \frac{\ell_{\max}+1}{\mathcal{H}\eta(x)} \Theta_{\ell_{\max}} + \tau' \Theta_{\ell_{\max}}. \quad (4.23)$$

This ensures that the high-order multipoles decay smoothly, preventing numerical artifacts. In the next milestone I employ an extremely valuable method known as line-of-sight integration, which lets us set $\ell_{\max} \sim 6-10$ and still obtain moderate to high accuracy. [word different?](#)

4.1.4. Polarization

In addition to the temperature anisotropies of the CMB, polarization also plays a significant role in constraining cosmological parameters. The CMB becomes polarized due to Thomson scattering, which selectively filters the radiation field and generates linear polarization when there is a local quadrupole anisotropy in the photon distribution.

The equations governing the polarization multipoles Θ_ℓ^P are similar to those for the temperature perturbations, but differ in their source terms and hierarchical coupling. It can be shown

that the full set of equations for takes the following form:

$$\Theta_0^P = -\frac{ck}{\mathcal{H}}\Theta_1^P + \tau' \left[\Theta_0^P - \frac{1}{2}\Pi \right], \quad (4.24)$$

$$\Theta_\ell^P = \frac{ck}{(2\ell+1)\mathcal{H}} \left[\ell\Theta_{\ell-1}^P - (\ell+1)\Theta_{\ell+1}^P \right] + \tau' \left[\Theta_\ell^P - \frac{1}{10}\Pi\delta_{\ell,2} \right], \quad 1 \leq \ell < \ell_{\max}, \quad (4.25)$$

$$\Theta_{\ell_{\max}}^P = \frac{ck}{\mathcal{H}}\Theta_{\ell_{\max}-1}^P - c\frac{\ell+1}{\mathcal{H}\eta(x)}\Theta_{\ell_{\max}}^P + \tau'\Theta_{\ell_{\max}}^P. \quad (4.26)$$

When including polarization in the perturbation calculations, eq. (4.16) no longer holds for the variable Π . Instead, it now includes contributions from the polarization monopole and quadrupole as well:

$$\Pi = \Theta_2 + \Theta_0^P + \Theta_2^P. \quad (4.27)$$

This modification accounts for the effect of polarization on the photon distribution and introduces additional terms in the Boltzmann hierarchy.

4.1.5. Neutrinos

Being nearly massless and only weakly interacting, neutrinos evolve differently from photons in the early Universe. While photons remain tightly coupled to baryons through Thomson scattering until recombination, neutrinos decoupled approximately one second after the Big Bang and have free-streamed almost unimpeded from then on. Their behavior is well-described by a perturbation to the neutrino temperature, similar to that of photons. Defining the fractional temperature perturbation as

$$\mathcal{N} = \frac{\delta T_\nu}{\bar{T}_\nu} \Leftrightarrow T_\nu = \bar{T}_\nu(1 + \mathcal{N}), \quad (4.28)$$

we find that the evolution of neutrino perturbations is exactly the same as that of photons in the absence of a collision term:

$$\frac{\partial \mathcal{N}}{\partial t} + \frac{ik\mu}{a}\mathcal{N} + \left(\frac{\partial \Phi}{\partial t} + \frac{ik\mu}{a}\Psi \right) = 0. \quad (4.29)$$

This equation shows that neutrino perturbations are only influenced by gravitational redshifting due to potential wells and cosmic expansion.

Since neutrinos are free-streaming, their distribution must be expanded into multipoles to describe their angular structure. Similar to the photon case, we may decompose the perturbation into Legendre multipoles:

$$\mathcal{N}'_0 = -\frac{ck}{\mathcal{H}}\mathcal{N}_1 - \Phi', \quad (4.30)$$

$$\mathcal{N}'_1 = \frac{ck}{3\mathcal{H}}\mathcal{N}_0 - \frac{2ck}{3\mathcal{H}}\mathcal{N}_2 + \frac{ck}{3\mathcal{H}}\Psi, \quad (4.31)$$

$$\mathcal{N}'_\ell = \frac{ck}{(2\ell+1)\mathcal{H}} \left[\ell\mathcal{N}_{\ell-1} - (\ell+1)\mathcal{N}_{\ell+1} \right], \quad \ell \geq 2. \quad (4.32)$$

Truncating this Boltzmann hierarchy at some maximum value $\ell_{\max,\nu}$ gives us then

$$\mathcal{N}'_{\ell_{\max,\nu}} = \frac{ck}{\mathcal{H}}\mathcal{N}_{\ell_{\max,\nu}-1} - c\frac{\ell_{\max,\nu}+1}{\mathcal{H}\eta(x)}\mathcal{N}_{\ell_{\max,\nu}}. \quad (4.33)$$

Neutrinos significantly influence cosmic structure formation. Their relativistic free-streaming contributes to the radiation density, altering the expansion rate and damping small-scale fluctuations. Additionally, neutrino free-streaming induces a phase

shift in the CMB power spectrum, providing a signature of their presence. Accurately modeling these effects requires truncating the Boltzmann hierarchy for neutrinos at $\ell_{\max,\nu} \approx 10 - 12$, capturing their impact more comprehensively than the photon case, where tight coupling allows for truncation at lower ℓ .

4.1.6. Cold dark matter

Cold dark matter (CDM) plays a crucial role in the formation of cosmic structure. Unlike photons and neutrinos, CDM particles are non-relativistic and interact only through gravity, meaning they do not experience pressure support or free-streaming effects. This leads to a different evolution for CDM perturbations, which gravitationally attract baryons and seed the formation of galaxies and large-scale structure.

The evolution of CDM density and velocity perturbations can be derived from the Boltzmann equation as well. Because dark matter does not participate in scattering interactions, its collision term vanishes, leaving us with the following equation governing its phase-space distribution function:

$$\frac{\partial f}{\partial t} + \frac{\partial f}{\partial x^i} \frac{\hat{p}^i}{a} \frac{p}{E} - \frac{\partial f}{\partial E} \left[H \frac{p^2}{E} + \frac{\partial \Phi}{\partial t} \frac{p^2}{E} + \frac{\partial \Psi}{\partial x^i} \frac{p\hat{p}^i}{a} \right] = 0. \quad (4.34)$$

Since CDM is non-relativistic ($E \approx m$), its evolution is primarily described by the first two moments of the Boltzmann equation—the density contrast and the velocity divergence—rather than a full hierarchy of multipole moments as needed for photons and neutrinos. By integrating over the momentum space, we obtain the continuity equation, which describes the conservation of CDM number density in an expanding Universe:

$$\frac{\partial n}{\partial t} + \frac{1}{a} \frac{\partial}{\partial x^i} (nv^i) + 3n \left(H + \frac{\partial \Phi}{\partial t} \right) = 0. \quad (4.35)$$

This equation closely resembles the fluid continuity equation, with additional terms accounting for the expansion of the Universe and the effect of gravitational potentials.

write as overdensity equation instead?

To describe the evolution of CDM velocity perturbations, we take the first moment of the Boltzmann equation, yielding the Euler equation:

$$\frac{\partial v^i}{\partial t} + H v^i = -\frac{1}{a} \frac{\partial \Psi}{\partial x^i}. \quad (4.36)$$

Since CDM is pressureless, it does not develop internal sound waves, unlike baryons, which are influenced by photon pressure before recombination. Instead, dark matter perturbations grow primarily due to gravitational instability, following the potential wells formed by initial fluctuations in the early Universe.

In Fourier space, the evolution equations for the CDM overdensity δ_{CDM} and velocity divergence v_{CDM} take the simpler forms:

$$\delta'_{\text{CDM}} = \frac{ck}{\mathcal{H}}v_{\text{CDM}} - 3\Phi', \quad (4.37)$$

$$v'_{\text{CDM}} = -v_{\text{CDM}} - \frac{ck}{\mathcal{H}}\Psi. \quad (4.38)$$

These equations highlight how CDM perturbations respond to metric fluctuations. The density contrast evolves due to velocity divergence and changes in the gravitational potential, while the velocity perturbation is sourced by gradients in the metric perturbation Ψ , analogous to how the Euler equation describes the motion of a perfect fluid affected by gravity.

4.1.7. Baryons

Having established the equations governing photons, neutrinos, and cold dark matter, the next step is to consider ordinary baryonic matter (electrons and protons). Since the number of baryons is conserved, the continuity equation follows directly from the dark matter case, as neither Coulomb nor Compton interactions affect baryon number conservation. Thus, the baryon number density satisfies

$$\frac{\partial n_b}{\partial t} + \frac{1}{a} \frac{\partial}{\partial x^i} (n_b v_b^i) + 3n_b \left(H + \frac{\partial \Phi}{\partial t} \right) = 0. \quad (4.39)$$

The key distinction from dark matter lies in the Euler equation, which governs momentum conservation. Unlike dark matter, baryons experience interactions that transfer momentum, particularly through the Thomson scattering of photons off electrons. The last term in the Euler equation for photons, derived earlier from the multipole expansion (see eq. (4.21)), and recall that $v_\gamma = -3\Theta_1$, accounts for this momentum transfer. Since momentum must be conserved between the baryons and photons, the baryon Euler equation must include a corresponding term weighted by the relative energy densities:

$$\frac{\partial v_b^i}{\partial t} + H v_b^i = -\frac{1}{a} \frac{\partial \Psi}{\partial x^i} - \tau' R (v_\gamma^i - v_b^i), \quad (4.40)$$

where R is the ratio defined in eq. (3.41).

As with other components, it is useful to take the Fourier transform to express the baryon evolution equations in terms of the density contrast δ_b and velocity divergence v_b . These take the standard form:

$$\delta_b' = \frac{ck}{\mathcal{H}} v_b - 3\Phi', \quad (4.41)$$

$$v_b' = -v_b - \frac{ck}{\mathcal{H}} \Psi + \tau' R (3\Theta_1 + v_b). \quad (4.42)$$

The presence of τ' indicates that prior to recombination, photons exert a significant drag force on baryons, preventing them from freely collapsing under gravity. Once recombination occurs and free electrons become scarce, τ' drops, allowing baryons to decouple from photons and fall into dark matter potential wells, ultimately leading to structure formation.

4.1.8. Metric perturbations

We have now established the perturbation equations for the different species in the Universe, and we finally arrive at the equations governing the metric potentials, Ψ and Φ . The first of these equations follows from the perturbed Einstein equations and describes how the time evolution of the metric perturbations is linked to the density perturbations in different components:

$$\Phi' = \Psi - \frac{c^2 k^2}{3\mathcal{H}^2} \Phi + \frac{H_0^2}{2\mathcal{H}^2} (\Omega_{\text{CDM}0} \delta_{\text{CDM}} + \Omega_{b0} \delta_b) e^{-x} + \frac{2H_0^2}{\mathcal{H}^2} (\Omega_{\gamma0} \Theta_0 + \Omega_{\nu0} \mathcal{N}_0) e^{-2x}. \quad (4.43)$$

derive this? This equation shows that the gravitational potential Φ evolves due to the curvature of space (Ψ term), gradients in the potential itself (the k^2 term), and contributions from cold dark matter, baryons, photons, and neutrinos.

The second equation we need provides a constraint relating Ψ and Φ . In the absence of anisotropic stress, general relativity dictates that $\Phi = -\Psi$. However, the presence of relativistic

species such as photons and neutrinos generates an anisotropic stress contribution, which modifies this relation:

$$\Psi = -\Phi - \frac{12H_0^2}{c^2 k^2 a^2} (\Omega_{\gamma0} \Theta_2 + \Omega_{\nu0} \mathcal{N}_2). \quad (4.44)$$

A key takeaway from these equations is that while Φ is dynamical and evolves due to matter and radiation perturbations, Ψ follows directly from Φ once the anisotropic stress contributions are known. This allows us to solve for the evolution of metric perturbations given the behavior of the matter and radiation components.

4.1.9. Inflation and initial conditions

To numerically solve the evolution of perturbations in the early Universe, we must specify initial conditions for all variables involved: the metric potentials, photon and neutrino multipoles, baryon and dark matter densities and velocities, and so on. But where do these initial fluctuations come from? **informal sentence?**

Inflation provides a compelling answer. During this epoch of accelerated expansion, quantum fluctuations in the inflaton field were stretched to cosmological scales. These fluctuations became classical perturbations and eventually seeded the large-scale structure of the Universe. The key prediction from inflation is the generation of a nearly scale-invariant Gaussian random field of curvature perturbations, which satisfies

$$\langle \mathcal{R}(\mathbf{k}) \mathcal{R}^*(\mathbf{k}') \rangle = (2\pi)^3 \delta(\mathbf{k} - \mathbf{k}') P_{\text{primordial}}(k). \quad (4.45)$$

Here, $P_{\text{primordial}}(k)$ is the primordial power spectrum, which is properly introduced in section 5.1.3 of the next milestone.

write different? Outside the horizon (i.e., for modes where $k \ll \mathcal{H}$), the curvature perturbation field \mathcal{R} remains approximately constant:

$$\frac{d\mathcal{R}}{dt} \approx 0. \quad (4.46)$$

This conservation law allows us to use \mathcal{R} as a bridge between inflationary predictions and initial conditions at later times.

In the Newtonian gauge, the curvature perturbation is defined as

$$\mathcal{R} = \Phi + \frac{\mathcal{H}^2 (\Phi' - \Psi)}{4\pi G(\bar{\rho} + \bar{P})} e^{-2x}. \quad (4.47)$$

For superhorizon modes in the radiation era, where metric potentials vary slowly, we have $\Phi' \approx 0$ and $\Psi' \approx 0$, and thus $\mathcal{R} \approx \Phi - \Psi/2$. Assuming $\mathcal{R} = 1$ thus sets the normalization for all other perturbation variables. The relation between the two potentials then becomes

$$\Phi + \Psi \approx -\frac{2f_\nu}{5} \Psi, \quad (4.48)$$

where

$$f_\nu = \frac{\Omega_{\nu0}}{\Omega_{\gamma0} + \Omega_{\nu0}}, \quad (4.49)$$

is the neutrino fraction. This yields the following initial conditions:

$$\Psi = \left(\frac{3}{2} + \frac{2f_\nu}{5} \right)^{-1}, \quad (4.50)$$

$$\Phi = -\left(1 + \frac{2f_\nu}{5} \right) \Psi. \quad (4.51)$$

For cold dark matter and baryons, the initial conditions become:

$$\delta_{\text{CDM}} = \delta_b = -\frac{3}{2}\Psi, \quad (4.52)$$

$$v_{\text{CDM}} = v_b = -\frac{ck}{2\mathcal{H}}\Psi. \quad (4.53)$$

For photons, we set:

$$\Theta_0 = -\frac{1}{2}\Psi, \quad (4.54)$$

$$\Theta_1 = \frac{ck}{6\mathcal{H}}\Psi, \quad (4.55)$$

$$\Theta_2 = \begin{cases} -\frac{8ck}{15\mathcal{H}\tau'}\Theta_1, & \text{(with polarization)} \\ -\frac{20ck}{45\mathcal{H}\tau'}\Theta_1, & \text{(without polarization)} \end{cases} \quad (4.56)$$

$$\Theta_\ell = -\frac{\ell}{2\ell+1}\frac{ck}{\mathcal{H}\tau'}\Theta_{\ell-1}, \quad \ell \geq 3, \quad (4.57)$$

and for photon polarization:

$$\Theta_0^P = \frac{5}{4}\Theta_2, \quad (4.58)$$

$$\Theta_1^P = -\frac{ck}{4\mathcal{H}\tau'}\Theta_2, \quad (4.59)$$

$$\Theta_2^P = \frac{1}{4}\Theta_2, \quad (4.60)$$

$$\Theta_\ell^P = -\frac{\ell}{2\ell+1}\frac{ck}{\mathcal{H}\tau'}\Theta_{\ell-1}^P, \quad \ell \geq 3. \quad (4.61)$$

The neutrino perturbations follow a similar hierarchy:

$$\mathcal{N}_0 = -\frac{1}{2}\Psi, \quad (4.62)$$

$$\mathcal{N}_1 = \frac{ck}{6\mathcal{H}}\Psi, \quad (4.63)$$

$$\mathcal{N}_2 = -\frac{c^2k^2(\Phi + \Psi)}{12H_0^2\Omega_{\nu 0}}e^{2x}, \quad (4.64)$$

$$\mathcal{N}_\ell = \frac{ck}{(2\ell+1)\mathcal{H}}\mathcal{N}_{\ell-1}, \quad \ell \geq 3. \quad (4.65)$$

These initial conditions, derived under the assumption of adiabaticity, allow us to evolve the Boltzmann system forward in time from a well-defined starting point. If one excludes neutrinos the equations above simplify accordingly, since $f_\nu = 0$.

should the initial conditions be derived?

4.1.10. The tight-coupling regime

Unfortunately, solving the full Boltzmann hierarchy numerically across all times is not practical—particularly in the early Universe, when Thomson scattering is extremely efficient and the optical depth derivative τ' is very large. In this limit, the equations become stiff and unstable for direct numerical integration. To avoid this issue, we may adopt a simplified set of equations valid in the so-called tight-coupling regime, where photons and baryons are so strongly coupled that they behave as a single fluid. These are derived under the assumption that time derivatives of $(3\Theta_1 + v_b)$ are suppressed and can be approximated via a leading-order expansion in $1/\tau'$.

By defining the combination

$$q = -\kappa[(1-R)\tau' + (1+R)\tau''](3\Theta_1 + v_b) - \kappa\frac{ck}{\mathcal{H}}\left[\Psi + \left(1 - \frac{\mathcal{H}'}{\mathcal{H}}\right)(\Theta_0 - 2\Theta_2) + \Theta_0'\right], \quad (4.66)$$

where the factor

$$\kappa = \left[(1+R)\tau' + \frac{\mathcal{H}'}{\mathcal{H}} - 1\right]^{-1}, \quad (4.67)$$

we may write the baryon velocity evolution as

$$v_b' = \frac{1}{1+R}\left[-v_b - \frac{ck}{\mathcal{H}}\Psi + R\left(q + \frac{ck}{\mathcal{H}}(-\Theta_0 + 2\Theta_2) - \frac{ck}{\mathcal{H}}\Psi\right)\right]. \quad (4.68)$$

The evolution of the photon dipole then becomes

$$\Theta_1' = \frac{1}{3}(q - v_b'). \quad (4.69)$$

Furthermore, the higher-order photon multipoles, as well as all of the polarization multipoles, are not dynamically evolved but instead algebraically determined from the dipole. More specifically, they can all be computed using the initial conditions in the normal regime (eqs. (4.56)-(4.61)). Furthermore, neutrinos are unaffected by baryon-photon interactions and therefore evolve the same way as usual.

As the Universe evolves and scattering between photons and electrons weakens, we eventually exit the tight-coupling regime. To determine when this transition occurs, we define a set of conditions that must be met simultaneously:

$$1. \left|\frac{d\tau}{dx}\right| > 10, \quad (4.70)$$

$$2. \left|\frac{d\tau}{dx}\right| > 10\frac{ck}{\mathcal{H}} \quad (4.71)$$

3. We have not yet passed the onset of recombination, which we take to occur at $x = -8.3$ (corresponding to $z \approx 4000$).

For each mode k , we start at the initial time and search forward to find when tight-coupling ends. This occurs when:

$$\left|\frac{d\tau}{dx}\right| = 10 \cdot \min\left(1, \frac{ck}{\mathcal{H}}\right). \quad (4.72)$$

If the solution gives $x > -8.3$, we fix the end of tight coupling to $x = -8.3$ instead. In practice, this only affects the smallest scales ($k \gtrsim 0.15 \text{ Mpc}^{-1}$), where tight coupling breaks earlier due to faster photon decoupling. At this point, we switch to solving the full Boltzmann hierarchy to accurately track the evolution of anisotropies around recombination.

rewrite? move to implementation?

4.1.11. Analytical approximations

While a numerical implementation is necessary for accurately solving the full system of cosmological perturbation equations, it's valuable to have analytical estimates to compare against. These approximations help ensure that the general trends in the evolution of our perturbations are physically reasonable and that no implementation errors have been made in the code. Even though we cannot solve the full Boltzmann hierarchy analytically, simplified solutions exist in specific limits and regimes.

One key check is to examine the evolution of the photon temperature monopole. Prior to recombination, when the photon-baryon fluid is tightly coupled, the evolution of the temperature perturbations can be approximated analytically. In the simplest case, we expect the combination $\Theta_0 + \Psi$ to oscillate sinusoidally:

$$\Theta_0 + \Psi \propto \cos\left(\frac{k\eta}{\sqrt{3}}\right), \quad (4.73)$$

which corresponds to acoustic oscillations in the photon-baryon fluid. Though this is a rough approximation, it captures the expected oscillatory behavior.

We can also validate the evolution of the gravitational potential Φ by comparing to known results in matter and radiation-dominated regimes. A useful consistency check is to simulate a Universe with only matter and radiation and examine the behavior of Φ on large (super-horizon) scales. For modes satisfying $k \lesssim 0.001 \text{ Mpc}^{-1}$, we expect:

$$\Phi_{\text{matter-era}} = \frac{9}{10} \Phi_{\text{radiation-era}}, \quad (4.74)$$

which reflects the transition from radiation to matter domination. Furthermore, a useful form for the evolution of the potential on subhorizon scales ($k \gtrsim 0.1 \text{ Mpc}^{-1}$) in the radiation era is:

$$\Phi \simeq \Phi_{\text{ini}} \frac{\sin(y) - y \cos(y)}{y^3/3}, \quad y = \frac{k\eta}{\sqrt{3}}. \quad (4.75)$$

Once inside the matter-dominated regime, the potential should become approximately constant in time, which can serve as another check.

Another important benchmark is the behavior of dark matter perturbations. On subhorizon scales during the matter era ($k \gg \mathcal{H}$), the Meszaros equation describes the growth of δ :

$$\delta \propto a = e^x, \quad (4.76)$$

while in the radiation era, where dark matter is not yet growing efficiently, we find $\delta \propto x$. An additional test is to compute the growth rate of perturbations, defined as:

$$f \equiv \frac{1}{\delta} \frac{d\delta}{dx} \simeq \Omega_m(x)^{0.55}, \quad (4.77)$$

which provides a useful reference in the matter-dominated epoch. correct that this is CDM? add subscript

have this in implementation?

4.2. Implementation details

4.3. Results and discussions

5. Milestone IV: Power Spectra

Having explored the background evolution of the Universe, its thermal history, and the growth of perturbations, we now reach the final step: computing the primary statistical observables in cosmology—the CMB power spectrum and the matter power spectrum. These spectra encode the evolution of perturbations from their initial conditions to their imprint on the cosmic microwave background and the large-scale distribution of matter. Their precise computation allows us to compare theoretical predictions with observations from missions such as Planck, placing stringent constraints on cosmological parameters.

The CMB power spectrum quantifies temperature and polarization anisotropies in the CMB sky, which arise from acoustic oscillations in the early Universe, gravitational redshifting, and scattering effects. To compute this spectrum, we must perform line-of-sight integration, tracing how photons have propagated from recombination to today, incorporating contributions from Sachs-Wolfe effects, Doppler shifts, and polarization terms. The matter power spectrum, on the other hand, describes how density fluctuations in the Universe are distributed across different scales today. It is derived from the total matter perturbations, including contributions from dark matter and baryons, and plays a crucial role in understanding the formation of large-scale structure.

By synthesizing the physics from all previous milestones, this milestone brings us to the final stage of our Einstein-Boltzmann solver. The results will allow direct comparison with observational data, testing the validity of our theoretical model and its numerical implementation.

TODO: shorten/word different to fit the rest

5.1. Theoretical framework

5.1.1. Temperature fluctuations as spherical harmonics

To begin understanding the CMB power spectrum, we must connect our theoretical results to the actual observable: the temperature fluctuations of the CMB across the sky. These are quantified by the temperature field $\Theta(t, \mathbf{x}, \hat{p})$ introduced in the previous milestone, which we already know how to solve for in Fourier space. Since the sky is a two-dimensional sphere, it is natural to expand this temperature field in terms of spherical harmonics:

$$\Theta(t, \mathbf{x}, \hat{p}) = \sum_{\ell=1}^{\infty} \sum_{m=-\ell}^{\ell} a_{\ell m}(t, \mathbf{x}) Y_{\ell m}(\hat{p}). \quad (5.1)$$

Here, $Y_{\ell m}$ are the spherical harmonic functions that form a complete basis on the sphere, and the coefficients $a_{\ell m}$ describe the amplitude of fluctuations at angular scale ℓ and azimuthal mode m . By expressing Θ in terms of its Fourier components we can compute these coefficients as

$$a_{\ell m}(t, \mathbf{x}) = \int \frac{d^3 k}{2\pi^3} e^{i\mathbf{k} \cdot \mathbf{x}} \int Y_{\ell m}^*(\hat{p}) \Theta(t, \mathbf{k}, \hat{p}) d\Omega_{\hat{p}}. \quad (5.2)$$

TODO: remove? rewrite to fit 4.17 and 4.18?

The multipole index ℓ is inversely related to the angular scale: low ℓ values correspond to large angular scales (broad patterns on the sky), while high ℓ values probe finer angular features. The m index corresponds to different orientations of the pattern at a fixed angular scale. However, since the Universe is assumed to be statistically isotropic, the ensemble average of the temperature field must be invariant under rotations. This implies that there should be no preferred direction on the sky, and hence no statistical dependence on m . Consequently, we define the angular power spectrum as the variance of $a_{\ell m}$ over m :

$$C_{\ell} \equiv \langle |a_{\ell m}|^2 \rangle = \frac{1}{2\ell + 1} \sum_{m=-\ell}^{\ell} |a_{\ell m}|^2. \quad (5.3)$$

Thus, the CMB power spectrum C_{ℓ} provides the average amplitude of temperature fluctuations as a function of angular scale ℓ , and is the primary quantity we compare to observations.

redundant?

A crucial point to emphasize is that we only observe one realization of the Universe. Theoretically, the average $\langle \cdot \rangle$ is meant

to be an ensemble average over many universes with the same statistical properties. In practice, we must replace this ensemble average with an average over the $2\ell + 1$ available m -modes at each ℓ , assuming ergodicity. This leads to a fundamental statistical limitation called cosmic variance. Since there are fewer m -modes at low ℓ , our estimate of C_ℓ becomes increasingly uncertain on large angular scales. The cosmic variance is quantified by

$$\frac{\text{Var}(C_\ell)}{C_\ell^2} = \frac{2}{2\ell + 1}, \quad (5.4)$$

which shows that the relative uncertainty is larger for small ℓ . Importantly, this is not a limitation of our instruments or data analysis, but a fundamental property of observing only one sky. As $\ell \rightarrow 0$, the number of independent modes becomes too small to robustly determine C_ℓ , leading to large uncertainties in the low- ℓ regime of the power spectrum.

5.1.2. Line-of-sight integration

To calculate the CMB angular power spectrum C_ℓ , we need the temperature multipoles $\Theta_\ell(k)$ at present time. A naive approach would be to evolve the full Boltzmann hierarchy for each ℓ up to some large $\ell_{\text{max}} \sim 1000$, which would involve solving thousands of coupled differential equations for every mode k . While this is theoretically feasible, it is extremely computationally expensive. Fortunately, a clever method known as line-of-sight (LOS) integration (see [add citation!](#)) offers an elegant and much more efficient alternative. Rather than evolving the entire Boltzmann hierarchy, this method instead solves for the monopole at all times and positions and then integrates over the photon path to determine the final anisotropies observed today. This drastically reduces the computational cost, requiring us to compute only a handful of lower multipoles, as mentioned in the previous milestone.

At the heart of the LOS approach lies the so-called source function, which captures all physical effects that contribute to the temperature anisotropies observed in the CMB. It is derived by formally integrating the photon temperature perturbation equation from the last milestone, and isolating the directional dependence through integration by parts and multipole expansion. The final expression for the temperature multipole at present time $x = 0$ is:

$$\Theta_\ell(k, x = 0) = \int_{-\infty}^0 \tilde{S}(k, x) j_\ell[k(\eta_0 - \eta)] dx \quad (5.5)$$

Here, $\tilde{S}(k, x)$ is the source function, and j_ℓ are spherical Bessel functions. Their appearance in the integral arises from the projection of three-dimensional spatial perturbations (characterized by wavevector magnitude k) onto the two-dimensional sky (characterized by angular multipole moment ℓ). These functions emerge naturally when decomposing the plane wave $e^{i\mathbf{k}\cdot\mathbf{x}}$ into spherical harmonics and radial functions, and encode how fluctuations in a Fourier mode k contribute to angular anisotropies at a given scale ℓ .

One can show that the source function itself is given by:

$$\begin{aligned} \tilde{S}(k, x) = & \tilde{g} \left[\Theta_0 + \Psi + \frac{1}{4}\Pi \right] + e^{-\tau}(\Psi' - \Phi') - \frac{1}{ck} \frac{d}{dx} (\mathcal{H} \tilde{g} v_b) \\ & + \frac{3}{4c^2 k^2} \frac{d}{dx} \left[\mathcal{H} \frac{d}{dx} (\mathcal{H} \tilde{g} \Pi) \right], \end{aligned} \quad (5.6)$$

Each term here has a specific physical interpretation: the first represents the monopole contribution (weighted by visibility), corrected by the gravitational redshift and polarization. Furthermore, $e^{-\tau}(\Psi' - \Phi')$ is simply the integrated Sachs-Wolfe (ISW) term, while the Doppler effect enters through the third term. The final term, involving Π , is a quadrupolar correction to the scattering due to anisotropic Thomson scattering, and includes polarization effects. In total, these terms encapsulate the full physics of how inhomogeneities in the early Universe source temperature anisotropies observed today.

5.1.3. Computing the temperature power spectrum

[rename section?](#)

Having computed the photon temperature multipoles $\Theta_\ell(k)$ through the line-of-sight integration method, we are in a position to extract one of the most important observables in modern cosmology: the angular CMB temperature power spectrum. This is computed by first squaring the photon temperature multipoles obtained via the LOS method (eq. (5.5)). We then multiply this with the primordial power spectrum mentioned in section 4.1.9 and integrate over all wave numbers k , which gives us:

$$C_\ell = \frac{2}{\pi} \int k^2 P_{\text{primordial}}(k) |\Theta_\ell(k)|^2 dk. \quad (5.7)$$

Fortunately, most of the simplest single field inflation models predict a so-called Harrison-Zel'dovich spectrum:

$$P_{\text{primordial}}(k) = \frac{2\pi^2}{k^3} \mathcal{P}_{\mathcal{R}}(k) = \frac{2\pi^2}{k^3} A_s \left(\frac{k}{k_{\text{pivot}}} \right)^{n_s-1}, \quad (5.8)$$

where A_s is the primordial amplitude, $n_s \sim 1$ is the spectral index, and k_{pivot} is a chosen reference scale. [explain origin?](#) Thus, using that the temperature multipoles $\Theta_\ell(k)$ must be real since they represent physical observables [correct?](#), we may rewrite eq. (5.7) as

$$C_\ell = 4\pi \int A_s \left(\frac{k}{k_{\text{pivot}}} \right)^{n_s-1} \Theta_\ell^2(k) \frac{dk}{k}, \quad (5.9)$$

Given the full theoretical C_ℓ spectrum, we can generate a synthetic realization of the CMB sky. This is interesting for comparing theory to actual observations, for visualizing the random nature of the CMB, and for generating mock data sets. However, to do this we must compute the coefficients $a_{\ell m}$ defined in eq. (5.2). A simple method for doing this is to sample them as complex Gaussian random variables with variance C_ℓ , i.e.,

$$a_{\ell m} = \sqrt{-\log(A)C_\ell} e^{2\pi i \theta}, \quad (5.10)$$

where A and θ are random numbers drawn from a uniform distribution over $[0, 1)$. To ensure that $T(\hat{n})$ is real-valued, we enforce:

$$a_{\ell, -m} = (-1)^m a_{\ell m}^*. \quad (5.11)$$

Once the $a_{\ell m}$'s are generated, the temperature map can be constructed using the HEALPIX library [add citation!](#), which perform the spherical harmonic synthesis efficiently.

[move/rewrite/specify in implementation?](#)

5.1.4. Features in the CMB

rename section? combine with previous?

The prominent peaks and troughs observed in the power spectrum arise from acoustic oscillations in the tightly coupled photon-baryon fluid before recombination. These oscillations are the result of competition between gravitational collapse and photon pressure in the early Universe. Overdense regions begin to collapse under gravity, but the intense radiation pressure from photons resists compression, resulting in oscillatory behavior analogous to sound waves.

From figure 3.3 presented in milestone II we know that the visibility function \tilde{g} is sharply peaked around recombination. A rough approximation is thus $\tilde{g} \approx \delta(x - x_{\text{rec}})$, which according to eq. (5.5) leads to

$$\Theta_\ell^{\text{today}}(k) \approx \left[\Theta_0 + \Psi + \frac{\Pi}{4} \right]_{\text{rec}} j_\ell[k(\eta_0 - \eta_{\text{rec}})] \approx [\Theta_0 + \Psi]_{\text{rec}} j_\ell(k\eta_0). \quad (5.12)$$

The second approximation follows from the fact that the anisotropy term is very small at recombination, and that $\eta_{\text{rec}} \ll \eta_0$. **word different?** Thus, we know that the dominant contribution to the observed anisotropies must come from the effective temperature perturbation at the time of recombination ($[\Theta_0 + \Psi]_{\text{rec}}$).

To understand how this perturbation evolves, we may consider the coupled evolution equations for the monopole and dipole in terms of the conformal time:

$$\frac{\partial \Theta_0}{\partial \eta} = -k\Theta_1 - \frac{\partial \Phi}{\partial \eta}, \quad (5.13)$$

$$\frac{\partial \Theta_1}{\partial \eta} = \frac{k}{3}(\Theta_0 - 2\Theta_2 + \Psi) + \frac{\partial \tau}{\partial \eta} \left(\Theta_1 + \frac{v_b}{3} \right), \quad (5.14)$$

Combining these equations (by differentiating the first and substituting into the second), we obtain a second-order differential equation of the form:

$$\frac{\partial^2(\Theta_0 + \Psi)}{\partial \eta^2} + \frac{k^2}{3}(\Theta_0 + \Psi) = F, \quad (5.15)$$

where the right-hand side acts as a driving force that includes contributions from higher-order multipoles and gravitational evolution:

$$F = \frac{2}{3}k^2\Theta_2 - k\frac{\partial \tau}{\partial \eta} \left(\Theta_1 + \frac{v_b}{3} \right) + \frac{d^2(\Psi - \Phi)}{d\eta^2}. \quad (5.16)$$

TODO: continue, mention most/all of the following:

1. Baryon loading
2. Radiation driving
3. Diffusion damping
4. Sachs-Wolfe plateau
5. Widths and relative heights of the first three peaks
6. The damping tail
7. Effects of reionization

TODO: maybe not focus on derivations?

5.1.5. Polarization spectra

TODO: write to fit milestone III

5.1.6. Effects of gravitational lensing

Gravitational lensing refers to the bending of light caused by the gravitational potential of massive structures between the source and the observer. As CMB photons from the last scattering surface travel through inhomogeneities in the large-scale structure on their way towards us, their paths are slightly deflected. This phenomenon introduces subtle distortions to the observed temperature and polarization anisotropies of the CMB. While the deflections are small, their cumulative effect leads to a measurable smoothing of the acoustic peaks in the observed angular power spectra by effectively redistributing power across multipoles. **word different?**

In order to compute the effect of gravitational lensing, we first need the CMB lensing potential C_ℓ^Ψ . This is found using LOS integration in the same way as the temperature multipoles (eq. (5.5)), with the source function being

$$\tilde{S}_\Psi = -\frac{2c\Psi}{\mathcal{H}(\eta_0 - \eta)} W(\chi, \chi_s). \quad (5.17)$$

where χ_s corresponds to the comoving distance to the last scattering surface. Here, the window function is

$$W(\chi, \chi_s) = \frac{S_k(\chi - \chi_s)}{S_k(\chi_s)}, \quad \text{for } \chi \geq \chi_s, \quad (5.18)$$

and zero otherwise, with the function $S_k(\chi)$ depending on spatial curvature k (see section 2.1.1):

$$S_k(\chi) = \begin{cases} \sin \chi, & k = 1, \\ \chi, & k = 0, \\ \sinh \chi, & k = -1. \end{cases} \quad (5.19)$$

rewrite to fit rest of text?

To quantify angular correlations in the CMB temperature anisotropies, we make use of the angular correlation function $C(\theta)$. This measures how the temperature fluctuations at two different directions \hat{n}_1 and \hat{n}_2 on the sky, separated by an angle θ , are statistically related. The theoretical prediction for this quantity is given by the Legendre series expansion:

$$C(\theta) = \frac{1}{4\pi} \sum_\ell (2\ell + 1) C_\ell P_\ell(\cos \theta). \quad (5.20)$$

However, the presence of massive structures alters this expression, leading to a lensed correlation function. This is approximately given by:

$$C^{\text{lensed}}(\theta) \approx \frac{1}{4\pi} \sum_\ell (2\ell + 1) C_\ell \exp \left[-\frac{\ell(\ell + 1)}{2} \sigma^2(\theta) \right] \times \left[P_\ell(\cos \theta) + \frac{\ell(\ell + 1)}{2} C_{\text{gl},2}(\theta) d_{1,-1}^\ell(\theta) \right], \quad (5.21)$$

where the variance

$$\sigma^2(\theta) = C_{\text{gl}}(0) - C_{\text{gl}}(\theta) \quad (5.22)$$

encodes the lensing-induced smoothing, and

$$C_{\text{gl}}(\theta) = \sum_\ell \frac{2\ell + 1}{4\pi} \ell(\ell + 1) C_\ell^\Psi d_{1,1}^\ell(\theta), \quad (5.23)$$

$$C_{\text{gl},2}(\theta) = \sum_\ell \frac{2\ell + 1}{4\pi} \ell(\ell + 1) C_\ell^\Psi d_{-1,1}^\ell(\theta). \quad (5.24)$$

In these expressions, d_{mn}^ℓ are the reduced Wigner functions:

$$d_{mn}^\ell(\theta) = \sum_i (-1)^i \frac{\sqrt{(\ell+m)!(\ell-m)!(\ell+n)!(\ell-n)!}}{(\ell+m-i)!(\ell-n-i)!i!(i+n-m)!} \times \cos^{2\ell+m-n-2i}\left(\frac{\theta}{2}\right) \sin^{2i+n-m}\left(\frac{\theta}{2}\right), \quad (5.25)$$

with the sum running over all integers i such that the factorials are non-negative. By integrating the lensed correlation function over all angles, we thus obtain the lensed power spectrum:

$$C_\ell^{\text{lensed}} = 2\pi \int_{-1}^1 C^{\text{lensed}}(\theta) P_\ell(\cos \theta) d \cos \theta. \quad (5.26)$$

rewrite to better the flow

mention what is useful about these quantities?

5.1.7. The neutrino power spectrum

In addition to photons, neutrinos also decouple early in the Universe's history and subsequently free-stream, carrying imprints of primordial perturbations. While we currently lack the observational capability to directly measure the anisotropies in the cosmic neutrino background, it is nevertheless possible to compute a theoretical neutrino power spectrum. This can be useful both for understanding their effect on the photon spectrum and as a consistency check within the Einstein-Boltzmann framework.

Neglecting higher-order multipoles such as the quadrupole, the source function for neutrinos can be written as:

$$\tilde{S}_\nu = (\mathcal{N}_0 + \Psi)\delta(\eta) + \frac{d\Psi}{dx} - \frac{d\Phi}{dx}, \quad (5.27)$$

The structure of this equation clearly shows that the neutrino spectrum receives contributions from both the SW term and the ISW term. The absence of the exponential optical depth factor $e^{-\tau}$, present in the photon source function, reflects the fact that neutrinos are unaffected by reionization or scattering processes.

merge into earlier sections?

5.1.8. The matter power spectrum

The matter power spectrum is a statistical tool that captures the distribution of matter density fluctuations across scales. It tells us how matter is clumped in the Universe at different spatial wavelengths, or equivalently, how different Fourier modes k contribute to the overall structure. The shape of this spectrum is determined by the primordial power spectrum generated during inflation, as well as the growth (or suppression) of structure depending on whether a mode is inside or outside the horizon. The latter also depends on whether the Universe is radiation or matter dominated, as we will see. word different?

The general form of the matter power spectrum is given by

$$P(k, x) = |\Delta_M(k, x)|^2 P_{\text{primordial}}(k), \quad (5.28)$$

where

$$\Delta_m(k, x) = \frac{2}{3} \frac{c^2 k^2 \Phi(k, x)}{\Omega_{m0} H_0^2} e^x, \quad (5.29)$$

is the transfer function representing the growth of matter perturbations over time. derive this?

TODO: maybe explain Meszaros effect

As with the CMB, it is most interesting to study the matter power spectrum today, since this is what we observe. It is then common to show k in units of h/Mpc and $P(k)$ in units of $(\text{Mpc}/h)^3$ because of degeneracies?. It is also helpful to mark the scale of matter-radiation equality,

$$k_{\text{eq}} = \frac{a_{\text{eq}} H(a_{\text{eq}})}{c}, \quad (5.30)$$

since this sets the transition between modes that entered the horizon during radiation domination versus those that entered later during matter domination.

TODO: change notation to fit milestone I

TODO: rewrite section to fit milestone III results

5.1.9. The correlation function

While the matter power spectrum is crucial for understanding structure evolution, it is sometimes more intuitive to consider its Fourier transform, the correlation function $\xi(r)$ in real space. This gives the excess probability (relative to a random distribution) of finding a pair of matter overdensities separated by a distance r , and is derived by using spherical symmetry to reduce the 3D Fourier transform to a 1D Hankel transform:

$$\xi(r) = \int_0^\infty \frac{\sin(kr)}{kr} \frac{k^3 P(k)}{2\pi^2} \frac{dk}{k}. \quad (5.31)$$

Alternatively, eq. (5.31) can be rewritten as a regular 1D Fourier transform by defining

$$f(k) = \frac{k P(k)}{4\pi^2} \quad (5.32)$$

and then using the identity

$$r\xi(r) = \int_{-\infty}^\infty f(k) e^{ikr} dk, \quad (5.33)$$

where we assume $f(k) = f^*(-k) = -f(-k)$ to ensure reality and symmetry. This form is numerically convenient for fast computations using, for instance, FFTLog. add citation?

A particularly significant feature in the correlation function is a bump at the sound-horizon scale r_{drag} . This is known as the BAO peak, and is a direct imprint of acoustic waves in the photon-baryon fluid before recombination. As we know from milestone II, baryons were dragged along with photons during the drag epoch due to their strong coupling, forming a pressure-supported sound wave that propagated outward from initial overdensities. When decoupling occurred, this sound wave “froze in”, leaving behind a characteristic excess of matter at a fixed comoving separation r_{drag} . In real space, this corresponds to a spherical shell of enhanced density, and in Fourier space, to oscillations in the matter power spectrum. don't make redundant

TODO: rewrite clumsy sentences

5.2. Implementation details

5.3. Results and discussions

6. Conclusions

References

Cort s, M. & Liddle, A. R. 2024, *Monthly Notices of the Royal Astronomical Society*, 531, L52

- Lewis, A., Challinor, A., & Lasenby, A. 2000, *The Astrophysical Journal*, 538, 473
- Nelson, D., Sharma, P., Pillepich, A., & et. al. 2020, *Monthly Notices of the Royal Astronomical Society*, 498, 2391
- Planck Collaboration, Aghanim, N., Akrami, Y., & et al. 2020, *Astronomy & Astrophysics*, 641
- Reid, R. Accessed: February 2025, Chi-squared distribution table with sigma values, <https://www.reid.ai/2012/09/chi-squared-distribution-table-with.html>
- Reiss, A. G., Scolnic, D., Anand, G. S., & et al. 2024, *The Astrophysical Journal*, 977, 120
- Tumlinson, J., Peebles, M. S., & Werk, J. K. 2017, *Annual Review of Astronomy and Astrophysics*, 55, 389
- Winther, H. A., Eriksen, H. K., Øystein Elgarøy, Mota, D. F., & Ihle, H. Accessed: February 2025, Cosmology II - A course on the formation of the cosmic microwave background and structures in the Universe, <https://cmb.wintherscoming.no/index.php>